STUDY ON WHITE ETCHING LAYER IN R260Mn RAIL STEEL BY THERMO-MECHANICAL SIMULATION

Hephzibah Murugan

TU Delft

Study of White Etching Layer In R260Mn Rail Steel By Thermo-Mechanical Simulation

By

Hephzibah Murugan

(4416112)

In partial fulfilment of the requirements for the degree of

Master of Science

in Material Science and Engineering

at the Delft University of Technology,

to be defended publicly on Wednesday June 13, 2018 at 2:00 PM.

Supervisors: Prof. Dr. ir. J. Sietsma

Dr. ir. J. Wu

Material Science Engineering Department

Faculty of Mechanical, Maritime and Materials Engineering

Delft University of Technology

TABLE OF CONTENTS

Acknowledgement

I am deeply grateful to my mentor Prof. Dr. Ir. Jilt Sietsma from TU Delft Material Science Engineering Department for giving me the opportunity to work on a challenging and extremely interesting research project. Due to his constant guidance, patience, encouragement and knowledge I have learnt a lot while working with this project. I thank Dr. Ir. Jun Wu from the Microstructure group in Material Science department for the supervision and guidance with experimental methods. I thank Prof. Dr. Ir. Roumen Petrov, Professor in Metals Technology, Ghent University, Belgium with the guidance on sample preparation methods. I thank Kees (C.) Kwakernaak for the help with EPMA analysis and during the SEM study. I thank the lab staff Sander van Asperen for the help in the Microscopy lab and Hans Hofman for the help with the GLEEBLE tests.

Lastly I am grateful to God, my parents, friends and fellow students for their patience, support, encouragement and love which helped me through the months spent to complete my research.

Abstract

Railway transport plays a vital role in a country's economic growth. Derailments result in loss of life, damage to rolling stock, service disruptions and harm the environment leading to the decrease in economic growth of a country. Improving train operating safety has been a high priority of the rail industry and the government. Train accidents occur as a result of many different causes; however, some are much more prevalent than others. One of the important causes for derailment is Rolling contact fatigue (RCF), which has gained more importance after the 1990's due to the several derailment accidents caused by it. Rolling contact fatigue is a group of rail damages that manifest themselves on the surface or near surface regions of the rail. RCF arises due to the rolling/sliding contact stresses that occur between rail and wheel leading to severe plastic deformation of the rail head with RCF cracks resulting in high maintenance costs. Another consequence of plastic deformation is the formation of white etching layer (WEL), a martensitic layer created from the deformed pearlite while the rail is in service. Effect of WEL is to reduce the resistance of rail steel to crack initiation because of its brittle nature.

In recent years, WEL has generated considerable research interests on its behavior under RCF conditions. Though most of the research carried out on WEL focuses either on the thermal or mechanical effects on its formation, little research has been carried out on the combined thermo-mechanical effects on WEL formation. In the present work, an attempt has been made to study the formation of WEL by thermo-mechanical simulation using the GLEEBLE thermo-mechanical simulator. Cylindrical samples prepared from the unaffected portion of the Dutch rail steel R260Mn were subjected to simultaneous deformation of maximum effective compressive strain of 3% and heating to maximum temperatures ranging from 650°C to 930°C. The simulation was carried out by varying the maximum temperature and no. of cycles. The metallurgical characterization of simulated WEL was performed using optical microscopy and scanning electron microscopy. The micro-hardness of WEL was studied using Vickers micro-hardness tester. The chemical composition of Mn was studied using electron probe microanalysis to ascertain the effect of Mn on band like formation occurred in samples processed at a certain temperature.

It is observed that the simultaneous heating and deformation increases the amount of WEL formed when compared to simulation by only heating. Hardness is found to increase with increase in temperature. When the no. of cycles increases the amount of WEL formation also increases. Simulation at very high temperature results in homogenous formation of WEL with negligible amount of untransformed pearlite.

CHAPTER ONE: INTRODUCTION

1.1 Impact of railroad on the world economy

Railway transport has become an important factor for a country's economic growth. [1] Railroad network have constituted for increase in technological progress from the nineteenth century across America, Europe and other parts of the world. The economic progress came with the steady increase in railways used as transportation mode for growing volume of goods and passengers. The railroad development also ignited progress in the steel production industry, civil engineering, engine construction, communications etc. [2]

The impact caused by the railroad network has been studied by many authors using different approaches and one such approach is called social savings which was studied by Fogel. Social savings is known as estimating the cost of transporting goods and people in one year with other best alternate freighting methods. Findings have shown that social savings have increased in developing countries which do not have good alternative transportation like waterways but also counties like America which also have well established alternate transport like waterways [1].

1.2 Railroad Maintenance and Derailment

Railroad maintenance is essential to withstand rail transportation productivity and safety. It helps to reduce costs while enhancing safety from any type of rail accidents. Increasing safety will also diminish risk of accidents which can cause loss of life of passengers and loss of goods. The lack of regular maintenance can cause rail deterioration and its related issues and can lead to train derailments [1].

The European Union Rail Agency in 2016 issued a report on the risks and accidents of trains due to collisions and derailments from 1990 to 2015 which is shown in Fig. (1.1). There has been significant improvement from the 1990's with a reduction in accident rate at 4% per year and the estimated average of fatal train collisions and derailments per billion train-kilometers was reduced from 4.8 in 1990 to 1.1 in 2015 [3]. A study commissioned by the European Rail Agency (ERA) on freight train derailment assessment and reduction of the risks from Det Norske Veritas (DNV) included data taken between 1996 and 2009 from 27 EU countries, Norway and Sweden and the main causes of derailment can be seen as infrastructure and rolling stock causes from the image. The breakdown of freight derailment causes are shown in the Fig (1.2) below [4].In the infrastructure category track geometry dominates to about 70% of the total cause. In the rolling stock category failure of axles estimates up to 40% of the cause. Though the derailments of trains have been reduced over the years according to report shown in figure 1.1, the cost of a single freight train derailment is about 1.1 million euro which increases the importance of the rail maintenance [4].

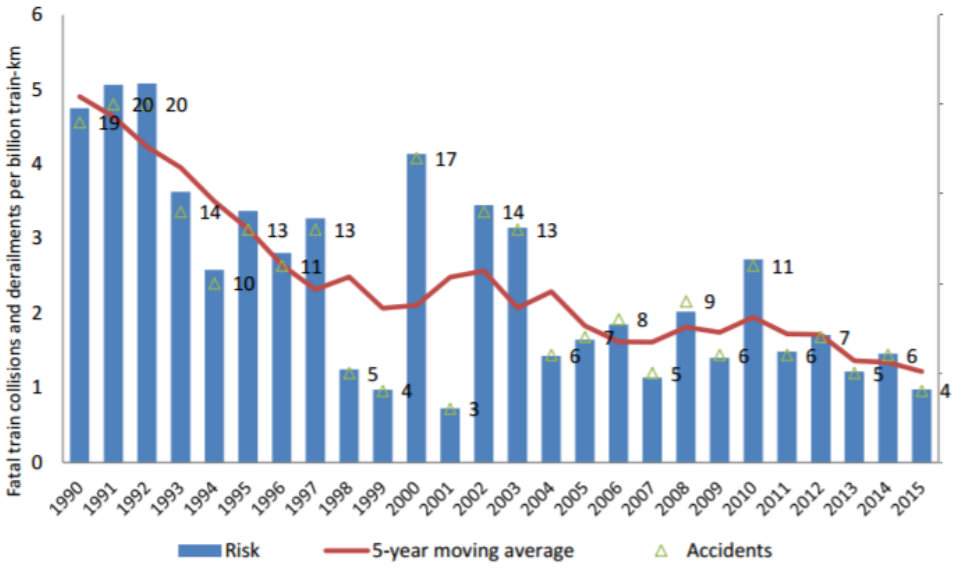

Fig 1.1: Fatal train collisions and derailments per billion kilometers for the EU-28 (Switzerland and Norway) for 1990-2015 [3]

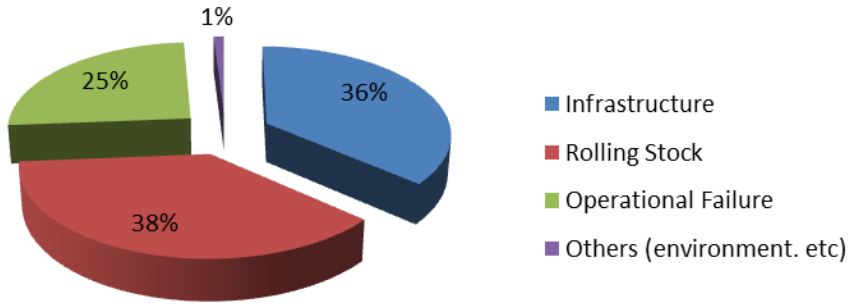

Fig1.2: Category of approximate breakdown of freight train derailment [4]

1.3 Failures in Dutch Railways system

Dutch railway has problems related to the stability of the track due to the Dutch sub-soil conditions especially in the western part of the country. Further the asset replacement costs are about 80 billion euros annually and consume about 60% of the annual maintenance costs and 75% of the renewal costs because of the usage and rapid degeneration patterns. The various causes of failures of turnouts are shown in Fig. 1.3 which shows one of the main causes of failure are defective parts which contributes to 22% of failures. Defects in the Dutch system appear due to the wheel-rail interaction which give rise to the rolling contact fatigue phenomenon (RCF), maintenance costs due to RCF resulted up to 30 million euros in 2005 (Prorail, 2005). [5]

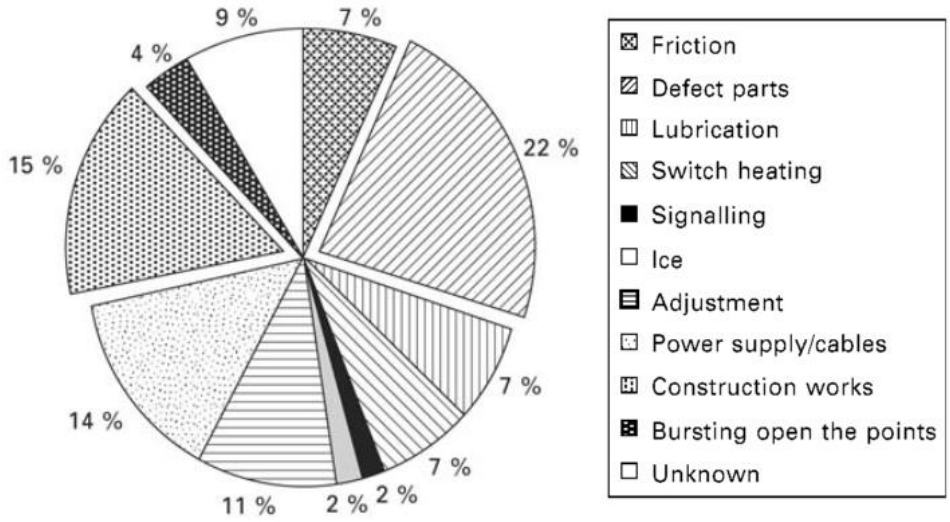

Fig. 1.3: typical causes of traffic disrupting failures for turnouts [5]

Though rolling contact fatigue has been recognized and measures been taken to reduce the damages caused by RCF, it has been actively referred to the Hatfield incident in UK that happened in October 2000 [5] when a passenger train traveling at 185km/hr, travelling over the high (outer) rail in a fairly mild curve (1500 m radius) derailed as the rail under the train shattered over tens of meters due to RCF cracks (Fig.1.4), this accident killed four passengers and injured 70 [6].

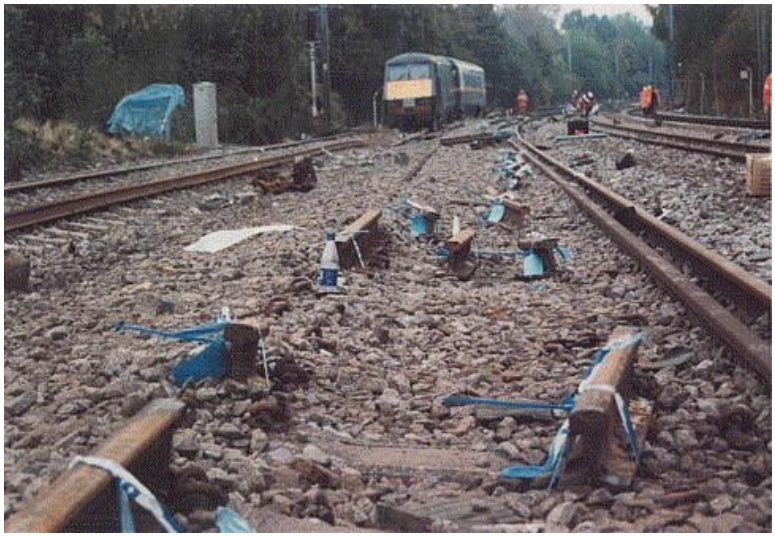

Fig 1.4: The crash site at Hatfield, showing disintegrated rail [6]

Other recent derailments related to rolling contact fatigue (RCF) include:

I. A train derailed in **Ellicott city, Maryland USA: August 20, 2012** as the rail at the point of derailment fractured due to defect across the rail that initiated at the

gauge corner head checks (region of rail in contact with the wheel throat). Other fractures followed over a 5m length breaking the rail into several fragments [7].

II. Train travelling at a speed of 27mph through a 9.1 degree curve derailed at **Columbus, Ohio USA: July 11, 2012** when the rail fractured under the train. Amongst the rail recovered 15 transverse defects were found on the rail the probable cause of the accident was a broken rail caused by rolling contact fatigue [7].

III. A freight train derailment at **Bates, South Australia: June 10, 2007** caused significant damage to the track and rolling stock. Investigation of the accident showed that a transverse rail defect caused the broken rail which led to the derailment [7].

IV. Thirteen cars derail at **Gainford, Alberta, Canada: October 19, 2003** derailed as the rail of the 550 m radius curve broke to pieces. The rail was found to have several transverse defects and showed signs of heavy surface fatigue [7].

V. Longitudinal cracking was found as the cause for derailment of a freight train due to the breaking of the rail at **Storsund-Koler, Sweden: May 11, 2013** [7].

Rails may break from many initial defects like crack that form at the base of the rail, bolt holes wheel burns etc. Breaks can also occur due to the crack propagation due to internal flaws from the manufacturing process and transverse cracks can propagate due to several factors such as track geometry, environment (especially cold weather) and rail material characteristics such as residual stress levels [7], in this study the transverse defects that arise due to rolling contact fatigue are focused and RCF and their types and their connection with white etching layers are explained in detail in the sections below.

1.4 Rolling Contact Fatigue

Various stresses that act on the rail that lead to many rail defects and failures are:

I. Bending stresses can occur when the applied vertical load causes the rail to bend between the sleeper supports which leads to longitudinal tensile stresses in the rail foot. The vertical load also makes the rail bend vertically on the web support which leads to longitudinal tensile stresses on the fishing surface [8].

II. Thermal stresses occur due to the thermal expansion and contraction of the long welded and continuously welded sections in the rail, when the temperature of the rail rises above or lowers below the stress free temperature at which the rails are welded. Compressive longitudinal stresses are present above the stress free temperature and tensile longitudinal stresses are present below the stress free temperature [8].

III. Residual stresses are introduced in the rail during the manufacturing process particularly during the straightening and head hardening processes. Localized residual stresses can occur through welding a section of rail because of the differential contraction and expansion of the metal [8].

An important form of stress which occurs due to the rail-wheel interaction is the rail contact stresses (Fig. 1.5a). The contact between the rail and the wheel is subjected to Hertzian contact stresses produced due to the contact and sliding contact conditions. This gives rise to fatigue crack propagation called as rolling contact fatigue and surface initiated defects which is called as rolling contact fatigue defects [8]. The various surface defects caused by RCF are gauge corner cracks, head checking and squats [9].

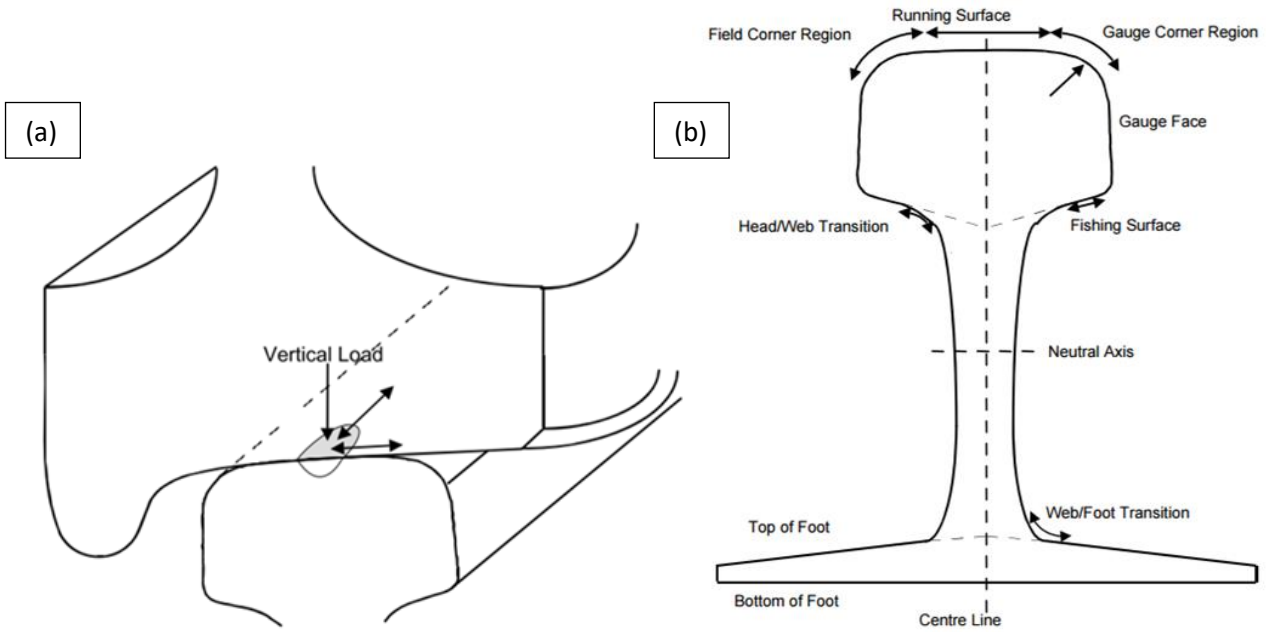

Fig. 1.5: (a) Rail contact stresses (b) Terminology used for rail locations [8]

Gauge corner cracks are thin cracks that appear at the gauge corner region (Fig. 1.5b) and can crop out mostly at the outer curves of the rails. They develop due to high wheel-rail contact stresses with coupled with large shear stresses because of the slip between the wheel and rail. Gauge corner cracks are noted to be regularly spaced and can occur for long lengths of a track or can appear in clusters (Fig.1.6b) [10]. Head checks is another type of RCF defect which can be found at the gauge corner region usually at the outer rail (Fig. 1.5b). They are mostly developed at curved tracks with radii less than 3000 m and in switches and crossings. They initiate as small cracks with shallow angle due to the contact stresses and grow with steeper angle and are capable of penetrating into the surface to about 30mm [11]. Gauge corner cracking is mostly distinguished from the head checks depending on where the cracks are located. If the cracks are located up to 10mm from the gauge face are gauge corner cracks and cracks that occur further from the rail crown are known as head checks(Fig. 1.6a)[12].

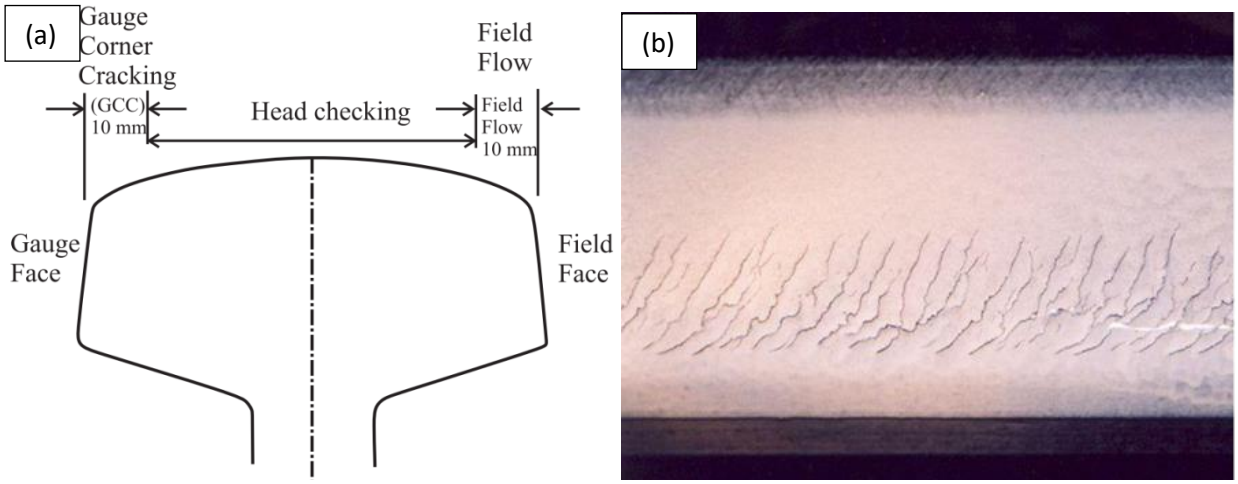

Fig. 1.6(a) Distinction between gauge corner cracking and head checking [11] (b) Gauge corner crack [12]

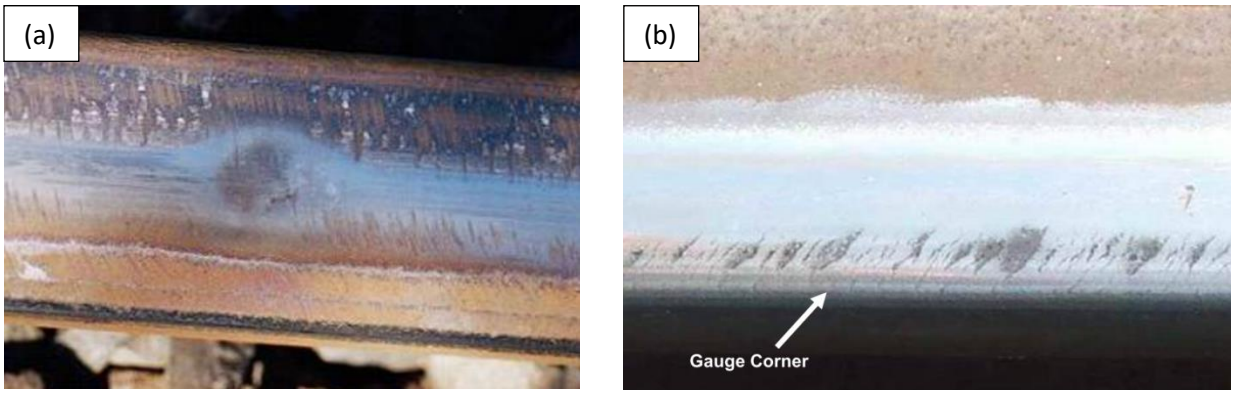

Fig. 1.7 Examples of RCF defects: (a) Running surface squat (b) Gauge corner squat

Squats are a type of rolling contact fatigue which occurs mostly in the Netherlands [13]. The International union of Railways identifies squats as "the widening and a localized depression of the rail/wheel contact band, accompanied by a dark spot containing cracks with a circular arc or V shape"[14] . The main characteristic of squats is plastic deformation and they are divided into categories of squats that usually occur such as gauge corner squats (Fig. 1.7b) they tend to initiate from pre-existing cracks which usually occur at the gauge corner but also are found at curves. The other type of squats are known as running surface squats (Fig. 1.7a) which are thought to form by thermal effects from rail friction associated with some form of microslip/slip and can occur anywhere in the running surface [8]. Squats are usually considered to be associated with white etching layer [14]. The structure and formation of the white etching layers and their various formation methods will be discussed in detail in the forthcoming sections.

1.5 White Etching Layer (WEL)

White etching layer is found to be present often but not always when a cross-section of rail containing squat is examined under the microscope [15]. The fig 1.8a shows the macroscopic top view of WEL, Fig. 1.8b shows the cross-section of the rail with a top WEL. It obtains its name as it is seen as a featureless white layer when it is viewed under the optical microscope after etched with 2-10vol% nital solution. The structure and properties, mechanism of formation of the white etching layers are discussed below.

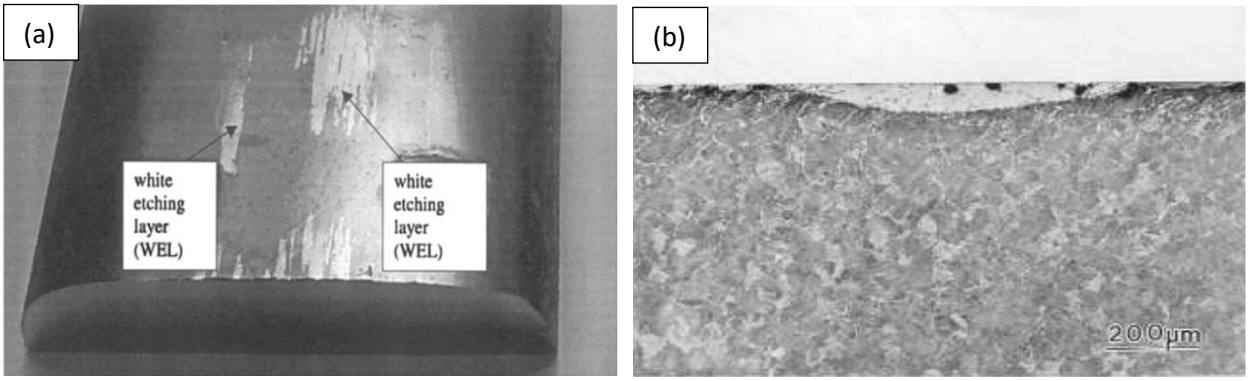

Fig. 1.8:(a) Macroscopic view of WEL on rail thread, (b) Transverse cross-section of (a) showing WEL in the upper layer [16]

1.5.1 Properties of WEL

The white etching layer is a brittle thin and hard layer formed on the surface of the rail, its typical feature is the distinct interface between the bulk material and its hardness is above 1000HV. This feature is associated with the rolling contact fatigue cracks. Many papers have questioned whether the white etching layer could be martensite because the hardness of WEL for a 0.24%C steel is about 1100HV as compared to the WEL formed by the conventional way of heating and quenching which is 500HV. Also another variation with the conventionally formed martensite and WEL is that the WEL was found to preserve its hardness up to its tempering temperatures of 800°C compared to conventional martensite which is tempered at temperatures less than 500°C studied by Kuznetsov et al [17].

1.5.2 Structure of WEL

The evidence of the white etching layer being martensite was found by Newcomb and Stobbs where a piece of rail was removed from an existing service track and studied using transmission electron microscopy (TEM) showed the white etching layer to be heavily deformed martensite with no carbides and were also unable to determine the lattice parameters [17]. Pyzalla et al. also found WEL to be martensite using the synchrotron X-ray scattering with some remnants of cementite particles. These white etching layers are also found in many other

circumstances such as cutting, deep drilling, grinding and reaming. White etching layer if found under various circumstances are either formed due to heating and quenching or a nanocrystalline structure formed due to severe plastic deformation [17]. The various type of white etching layer summary is given in Table:1.

The difference between the study by Newcomb and Pyzalla is that Newcomb proposed that the WEL structure could be formed due to the plastic deformation of the rail surface especially at the asperities which would introduce large number of dislocations and also involve breaking and dissolution of the cementite platelets into ferritic martensite, which is ferrite supersaturated with carbon, this also exhibits micro-twinning which is a martensitic feature. Many other papers talk about WEL formed by plastic deformation where Minouru *et al*.[18] studied the WEL formation by ball-milling and ball drop deformation. Both the methods show the formation of a nanocrystalline structure and dissolution of cementite along with presence of spherodization. Study by R.I. Carroll and J.H Beynon by twin disc method where two discs roll in the same direction in this case at 1500MPa for 5s creating a rolling/sliding motion which resulted in the formation of WEL due to plastic deformation [19].

1.5.3 Formation mechanism of WEL

The study by Pyzalla *et al*. on WEL by rapid heating and quenching cycle using laser treatments on steel showed that the WEL formed to be martensitic with tetragonal distortions in the bcc crystal lattice. Similar study done by Jun Wu et al.[20] showed the morphology of the WEL simulated to be similar to the rail WEL formed naturally. The study also found the influence of hydrostatic pressure in shifting the eutectoid carbon composition from 0.71wt%C to 0.48wt%C , this causes a shift in the eutectoid transformation temperature which is usually a minimum of 700°C to 670°C .This means when enough hydrostatic pressure is present between the rail and wheel contact, the rail composition is shifted from (near) eutectoid to hypereutectoid [20]. Takashi *et al*. [21] studied the white etching layer using Atom Probe Tomography (APT) and proposed that the WEL region did not undergo heavy plastic deformation. He mentioned this from analysis on Mn enriched zones corresponding to previously existing cementite lamellae. Also, the large temperature rise predicted by frictional heating calculations in the wheel-rail contact region by shape analysis confirmed the frictional heating of the manganese enriched zones. Altogether the observation of unchanged cementite interlamellar distance in the rail surface pearlite, the absence of work- hardened pearlite zone beneath the WEL moves towards the direction that- WEL is formed by martensitic phase transformation after rapid austenization by frictional heating [21].

In this thesis the WEL formation is simulated by both plastic deformation and heating simultaneously in laboratory conditions by a thermo-mechanical simulator. The simulated WEL is compared with the WEL observed in rails and the WEL simulated by Jun Wu et al. [20] by

using only heating for the phase transformation to martensite. Similarities will be discussed based on the observations and with literature data available.

Table1: Summary of white etching layer formation mechanisms

Mechanism of formation	White etching layers
WEL formed by plastic deformation	• TEM study reveal heavily deformed martensite [17] • Nanocrystalline structure formation by ball milling and ball drop deformation [18] • Simulation of WEL by twin disc method [19]
WEL formed by heating and quenching	• Synchrotron XRD reveal tetragonality and retained austenite in WEL [17] • Simulation of WEL by laser heating [17]. • Thermo-mechanical simulation of WEL [20] • Formation of WEL resulting in absence of work-hardened pearlite and unchanged cementite lamellar distance revealed by APT results[21]

1.6 Aim of the Thesis

White etching layer has become an area of interest due to the high maintenance costs that occur by the presence of WEL in rail. It is also studied so that the rail operating safety can be increased. The various studies done previously on WEL was to study the microstructure of WEL formed on a rail in service, few studies are conducted on rail which mimic the real life situation suitable for rail formation such as the twin disc . The aim of this thesis is to simulate WEL by simple laboratory environment by simultaneous heating and deformation and study the effects of heating and deformation on WEL and also compare it to the WEL simulated by the same conditions by heating.

CHAPTER TWO: EXPERIMENTAL METHODS

2.1 Materials and Experimental Procedures

The steel grade chosen here is R260Mn rail steel, the chemical composition of the steel is 0.64%C, 1.51%Mn, 0.25%Si, 0.02%P and 0.02%S (mass%). [13] The reference pearlite steel (Fig. 2.1a) also known in the thesis as base pearlite termed so as it is the initial microstructure which will undergo simulation. The base pearlite is seen as both dark and light regions and at higher magnification the pearlite lamellae feature can be seen in Fig. 2.1b. The lamellae features of the pearlite are observed clearly in the SEM images (Fig. 2.2).

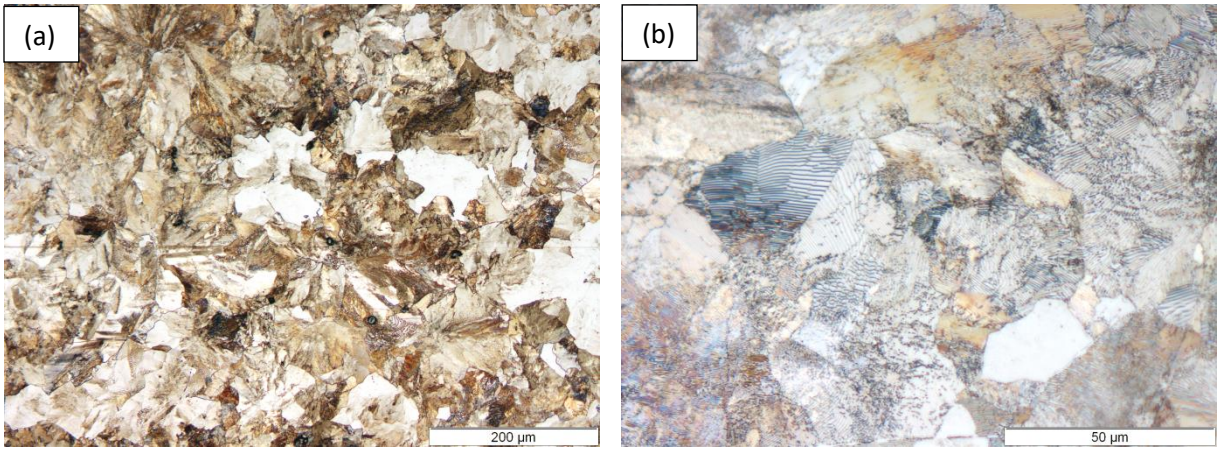

Fig. 2.1 Optical Micrograph of base metal showing pearlite at: (a) 100x, (b) 200x

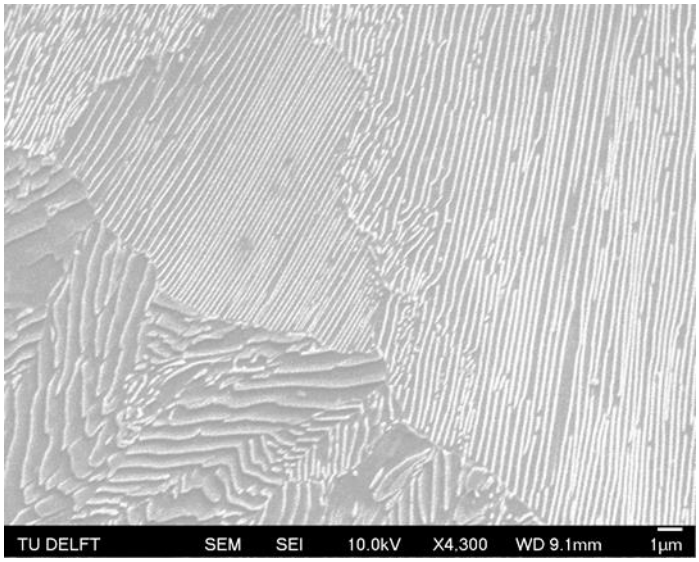

Fig. 2.2 SEM image of the base metal showing pearlite

2.2 Characterization Techniques

The white etching layer was simulated in the laboratory using the thermo-mechanical simulator the Gleeble1500. Various post-processing techniques such as Vickers Hardness, optical microscopy (OM), ImageJ analysis and scanning electron microscopy (SEM) were done to study the cross-section and hardness of the processed samples. The various characterization techniques mentioned are explained in detail in this section.

2.2.1 Thermo-Mechanical Simulator (GLEEBLE 1500)

The thermo-mechanical simulator is used here to simulate the white etching layer. The Gleeble 1500 (Fig.2.3) is equipped to administer precise heating and quenching in an inert or vacuum atmosphere. It is designed to apply heating by passing electric current from one ram to the other through the sample [22]. The heating system is also equipped with signal feedback by thermocouple to provide precise control of the heat treatments of the specimens tested.

The Gleeble has a fully integrated servo-hydraulic system which allows exerting force in tension or compression [23]. The Gleeble also allows various heating and cooling rates which can be used to produce different microstructural results. The mechanical simulator apparatus is connected to a control computer which can measure stroke, strain (engineering and true), stress (engineering and true) and temperature. The control computer is also capable of using inputs from pyrometers, dilatometers and various strain gauge devices [24].

Fig. 2.3 Photograph of the thermo-mechanical simulator GLEEBLE1500 for current study

2.2.2 Metallographic Sample Preparations

After the samples are processed in the Gleeble, the samples fitted with the single thermocouple are cut at the centre of the effective length to expose the cross-section. This is shown in Fig 2.4 below.

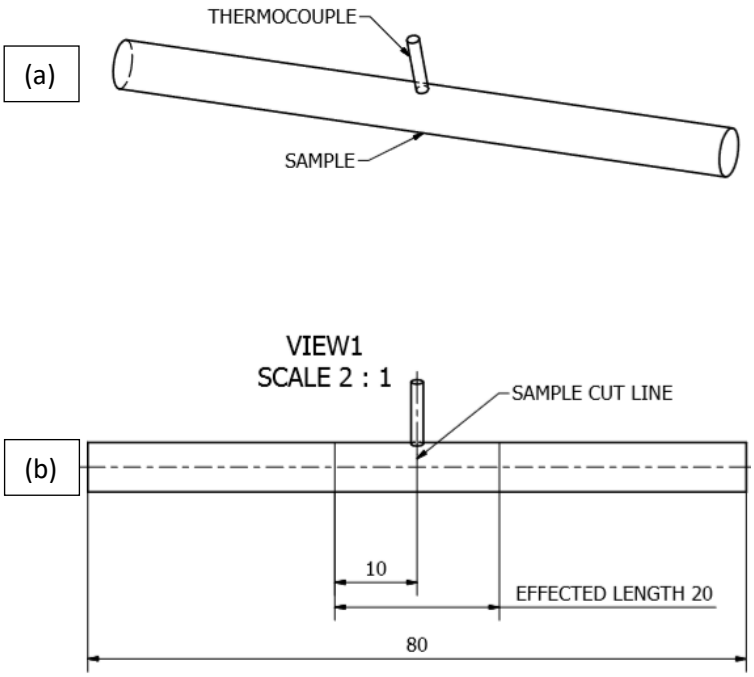

Fig. 2.4 (a) 3D view of the sample with the thermocouple (b) 2D view of effective length and cut line

The sample after simulation is cut at the sample cut line (Fig. 2.4b) to expose the cross-section and this cut portion is further processed by grinding using the sequential Struers number 320#, 800#, 1200#, 2000# grinding papers in a semi-automatic grinding machine (Struers LabPol-21) shown in Fig.2.5.

Fig. 2.5 Photograph of the grinding machine

The grinding process was followed by wet polishing using diamond suspension of 3µ and 1µ solution using the mol cloth and nap cloth respectively to obtain a polished surface without scratches and dirt. The polishing machine used (Struers LabPol-5) is shown in Fig. 2.6.

Fig. 2.6 Photograph of the polishing machine

2.2.3 Optical Microscopy (OM)

The polished specimen is then etched for a few seconds with 5% nital solution and the surface structure was first studied using the optical microscope (Olympus BX-60). The structure of the microscope is schematically shown in Fig. 2.7a.

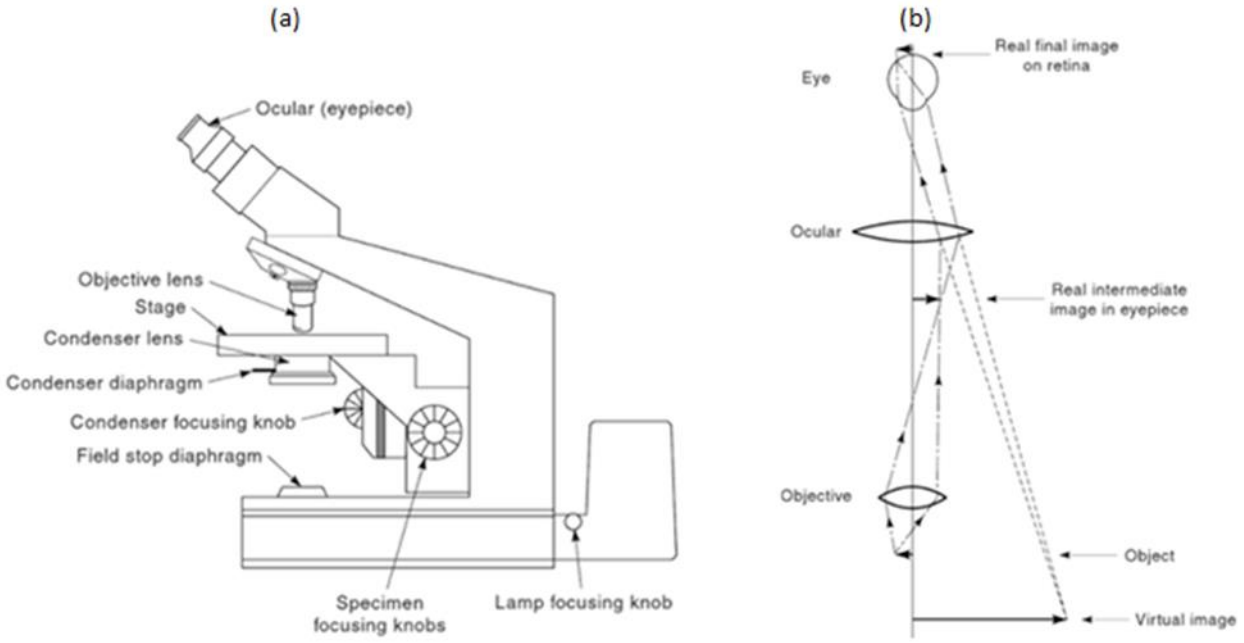

Fig.2.7 optical microscope: (a) parts (b) perception of magnified virtual image [25]

The optical microscope has two main components: objective lens and condenser lens. Some of the other components in the optical microscope are eyepiece (ocular), stage, condenser diaphragm and specimen focusing knobs etc. which are also shown in the Fig. 2.7a.The working of the optical microscope is such that when a specimen is viewed in the microscope, visible light is used to illuminate the sample surface, the condenser lens focuses light from an illuminator onto the sample and the objective lens collects light diffracted from the specimen and forms a magnified image near the eyepiece. The final magnified images of the specimen surface are projected onto the retina of the eye or onto an imaging surface. This mechanism is shown in Fig. 2.7b [25].

The optical microscope used for this study is the Olympus BX-60 which is shown in the Fig. 2.8 below.

Fig. 2.8 Photograph of the optical microscope at TU Delft

2.2.4 Vickers Hardness (HV)

The Vickers hardness measurements are used to reflect the mechanical properties due to the changes that occurred during the thermo-mechanical simulation. The hardness of the specimens is studied using the Vickers micro-hardness testing machine. The micro hardness machine has a diamond indenter in the form of a pyramid with a square base at an angle of 136° between the opposite faces as shown in Fig. 2.9a [26] . In the current study loads such as 0.05kgf and 0.1kgf are usually applied for 15 to 30 seconds [27]. When a suitable load is applied on the specimen the pyramid shaped indenter leaves a mark, the diagonal of the impression

left by the indenter are measured using a suitable microscope and the Vickers hardness is measured using the formula [26]

$$[HV] = 1854.4L / d^2$$

Where L = load in N

d= average of the diagonal in μm [27]

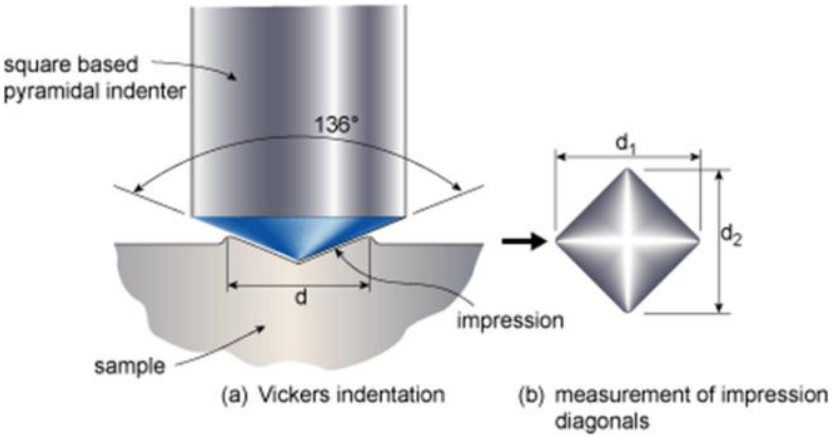

Fig. 2.9: (a) Vickers indentation and (b) top view of the indentation [28]

The micro-hardness is tested using the Struers Durascan70 which is shown in Fig. 2.10 below.

Fig. 2.10 Semi-automatic Vickers hardness tester at TU Delft

2.2.5 Scanning Electron Microscopy (SEM)

Due to the very fine cementite inter-lamellar distance and the complex structure of WEL, the optical microscope is unable to fully resolve the microstructure in the pearlite and WEL; in this case the scanning electron microscopy is used due to improved spatial resolution. The main components of the SEM are schematically shown in the figure 2.11. Electrons are produced by a field emission electron gun which is a tungsten wire with a sharp tip less than 100nm. In the current thesis the electrons are then accelerated to a voltage between 1 and 40kv [29]. The electron beam is subsequently de-magnified, converged and focused by a series of objective and condenser lens before reaching the surface of the sample as a nanometer sized spot. The electron beam gradually scans the specimen surface and is controlled by the scanning coil. The interactions between the electron beams and the specimen generate signals and these emitted signals are collected by detectors which form the available imaging mode in SEM [30].

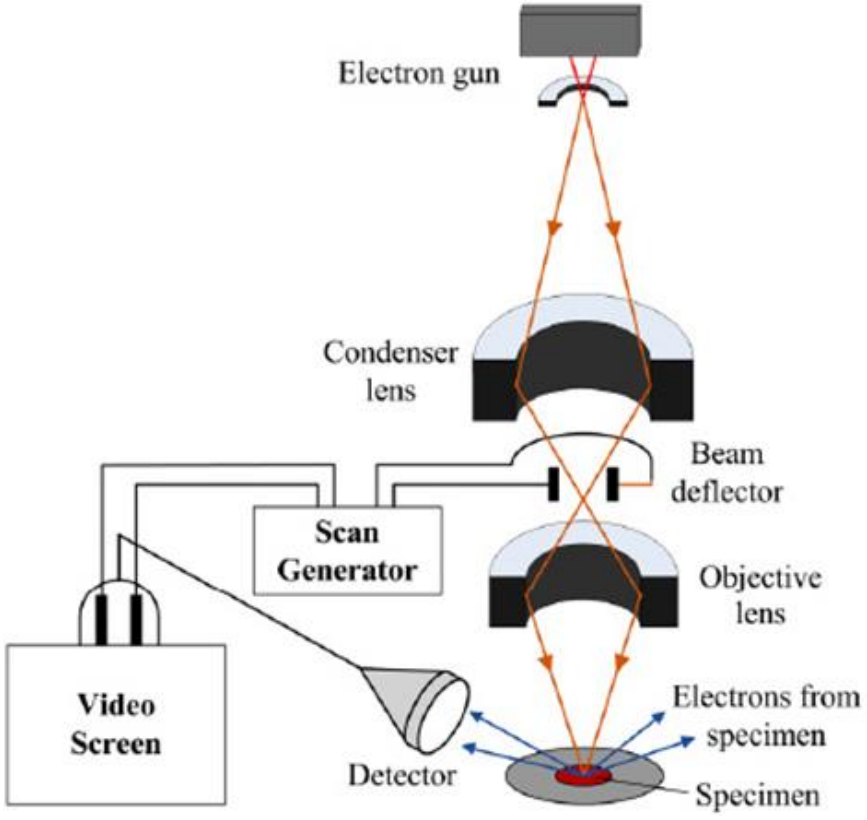

Fig. 2.11 Principle of Scanning Electron Microscopy (SEM) [31]

Some of the different signals emitted when the incident electron beam that hits the sample are the Auger electrons (AE), back scattered electrons (BSE), electron back scatter diffraction (EBSD), secondary electrons (SE), characteristic x-rays etc. shown in Fig. 2.12. The Auger electrons and characteristic x-rays are used to study the chemical composition of the sample. BSE can be used for imaging the morphology of the sample but is more efficient in analyzing the different elemental distribution in the sample as its resolution for morphology is

too low [32]. EBSD is used to determine the crystal structures and orientation of minerals [33]. Transmitted electrons are used in transmission electron microscopy (TEM) which provides information about the sample's inner structure [34]. Secondary electrons originate from close to the surface or at the surface of the sample due to inelastic interaction between the incident beam and the sample. They have lower energy than compared to BSE and are very useful to study the topography of the sample. In this current study the SE are used to study the phases present in the sample after simulation. The structure characterization was done using the JOEL JSM-6500F Field Emission Scanning Electron Microscope as shown in the Fig. 2.13. The scans are done in this thesis with voltage between 10 – 15 kv, current of $6x10^{-11}$ A and working distance between 8-9 mm.

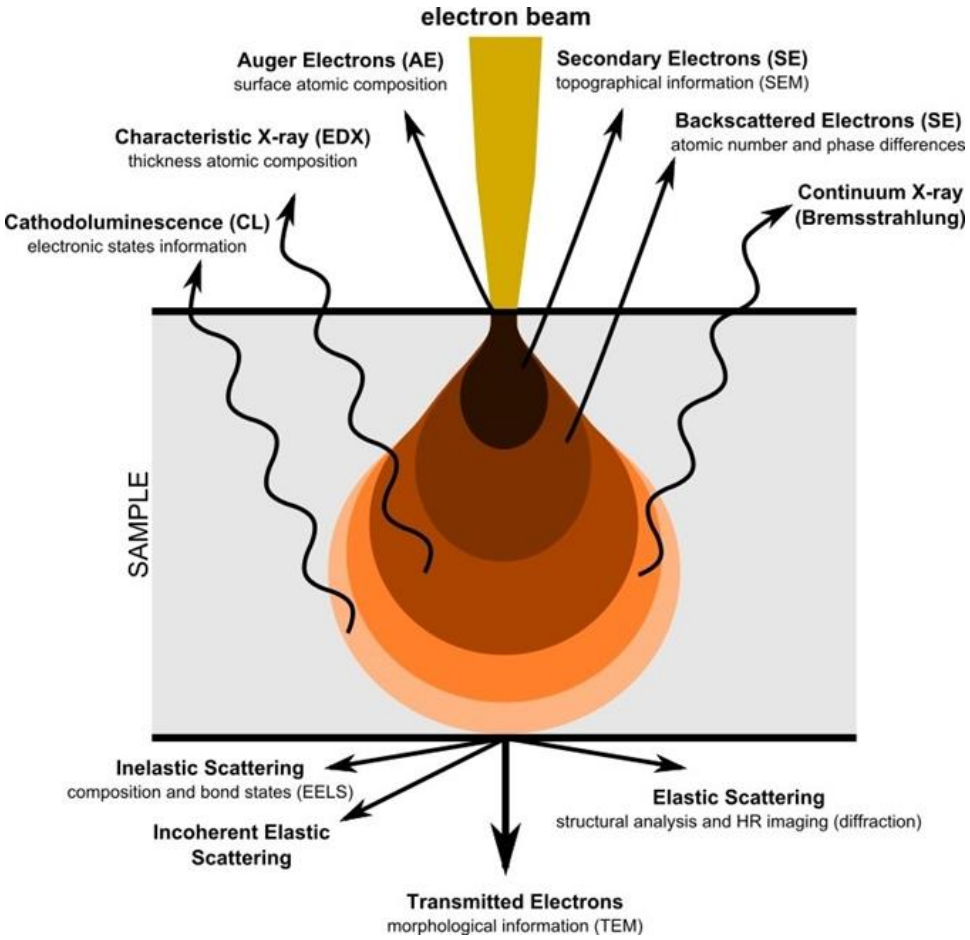

Fig. 2.12 Depth of quantum emission and special resolution [35]

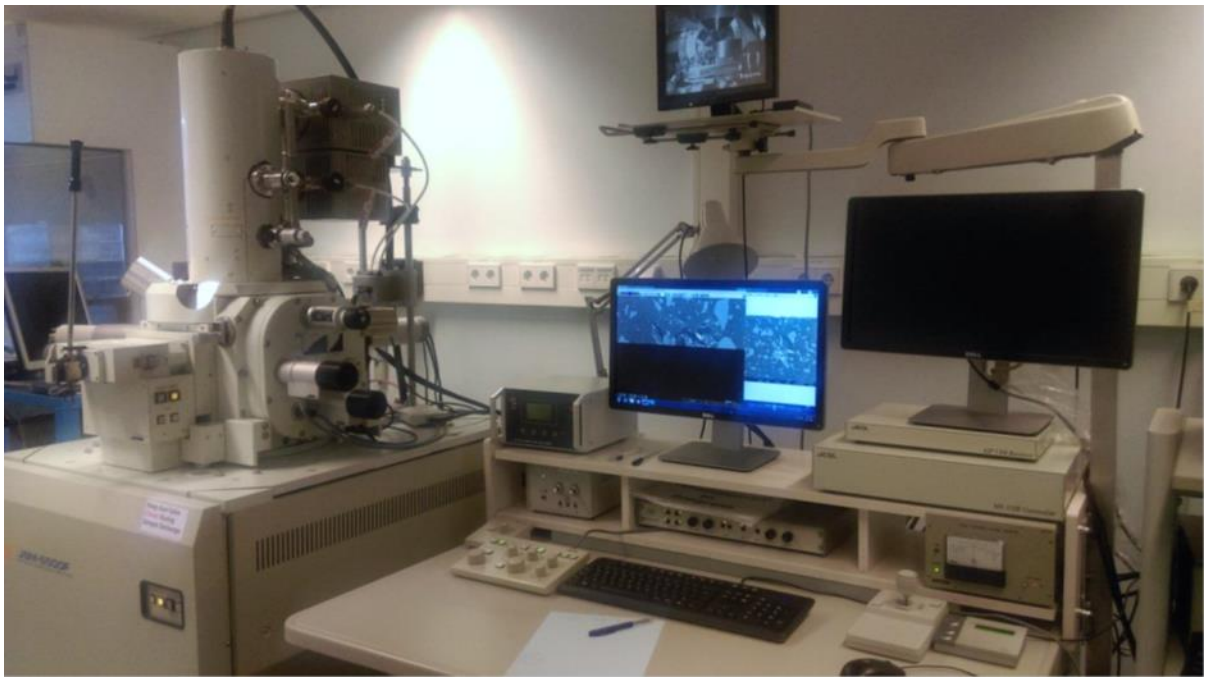

Fig. 2.13 SEM at Technical University Delft (JEOL JSM-6500 F)

2.2.6 Electron Probe MicroAnalysis (EPMA)

Electron probe microanalysis referred as “EPMA” is a non-destructive in-situ analytical method to determine the chemical composition of major elements to trace elements in solid specimens. EPMA is very similar to scanning electron microscopy with added capability of chemical analysis. A beam with high energy electrons is focused on to a sample which is to be tested; this beam that hits the sample generates x-rays corresponding to the elements in the sample. The energy and the intensity of the x-rays emitted from the sample are analyzed using the Wavelength Dispersive Spectroscopy (WDS) or Energy Dispersive Spectroscopy (EDS). Usually WDS is used for chemical analysis as it is more efficient than EDS. This analysis can be done to qualitatively deduce the chemical composition of the sample at very small “spot” sizes (as small as 1-2 microns) [36, 37]. The setup for the EPMA is shown in Fig. 2.14 consists of an electron gun which is the source of the electron beam. The electromagnetic lenses focus the beam onto the target specimen. An optical microscope coaxial to the electron beam has variable magnification which identifies the point of interest on the specimen. The wavelength dispersive spectrometer is made of crystal monochromator and an x-ray detector is placed in such a way to impinge the x-rays that fall on the crystal and are dispersed. The dispersed x-rays are examined to determine the composition of the sample [38, 39]. In this current study the measurement was performed using JEOL JXA 8900R microprobe with beam energy 10keV, beam current of 10nA employing WDS.

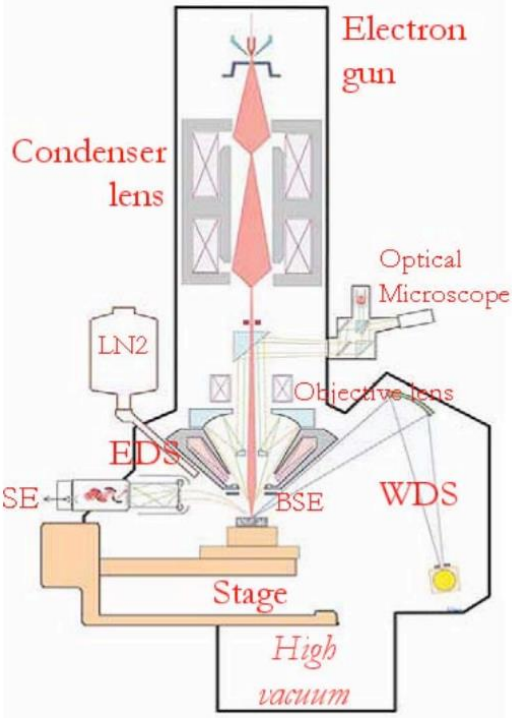

Fig. 2.14 Schematic of EPMA [40]

2.2.7 ImageJ

Further processing of the SEM images and optical microscopy images are done by the ImageJ software. ImageJ is a public domain Java image processing program. It can be used to edit, analyze, display, process, save and print 8-bit, 16-bit and 32-bit images and supports images in formats such as TIFF, GIF, JPEG, BMP, DICOM etc. The software is eligible to measure pixel value statistics of user defined regions and intensity threshold objects. ImageJ can also measure area of a selected region, distance and angles. It also supports standard image processing methods such as contrast manipulation, sharpening, smoothing, edge detection and median filtering. It also allows transformations such as scaling, rotation and flip, all analysis and processing actions are allowed at any magnification factor [41].

The functions in Imagej are essential in analyzing the spheroidization of cementite and quantifying the phases present in the sample after the experimental processing. Quantification of the martensite (WEL) and untransformed pearlite is studied using the digital microscope images of the overview of the cross-section of the sample seen in Fig. 2.15. Fig. 2.15a shows the cross-sectional overview of sample $X_{700\text{-}5}$. In Imagej the colour thresholding selection under image option in the tool bar is used to select the light or dark regions which correspond to martensite and pearlite. Example of selection of light region is seen in Fig. 2.15b, The selection is applied in the image and the area is calculated using the measure option in the tool bar under the option analyze. The calculated area of the different regions by the total area of the cross-section gives the amount of the certain regions present in the sample. The spheroidization of

cementite is analyzed from the SEM images at more or less the same magnification. The chosen SEM images are filtered using the bandpass filter tool to remove shading and provide smoothing for the selected image (Fig. 2.15c). The large martensite regions if present are removed as shown in Fig. 2.15c to avoid errors in the quantification. The cementite platelets and the spheroidized particles are studied using the 3:1 aspect ratio criteria mentioned in literature [42]. According to the method discussed by Chattopadhay et.al [43] the volume fraction of carbide plates present is a selected area calculated is known as "V_c", using the aspect ratio the volume fraction of spheroidized particles is calculated using the analyze particles option in imagej which is known as "V_s" (Fig. 2.15d). From both the volume fractions the volume percentage of spheroidized particles is found.

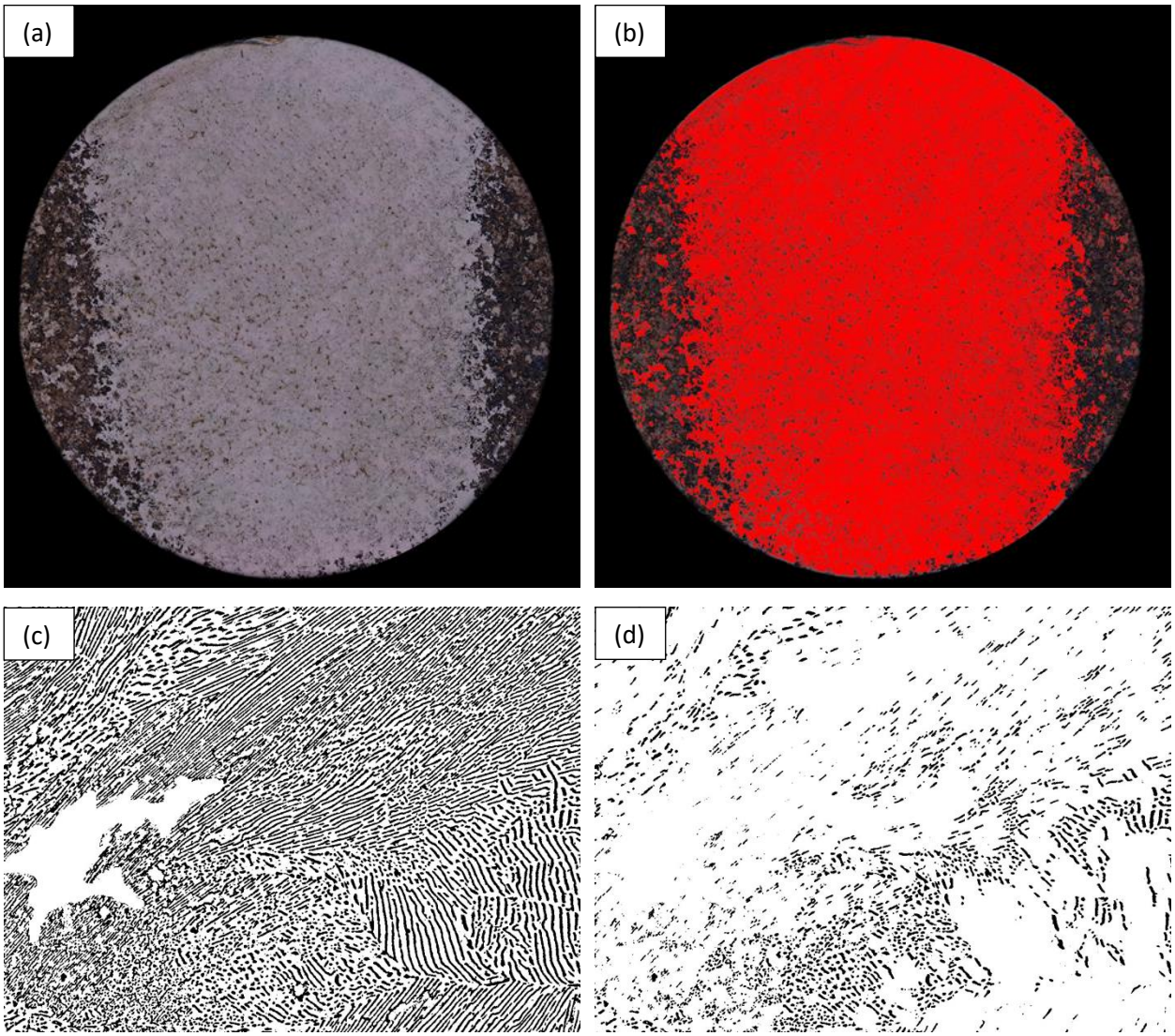

Fig. 2.15 Example of processing of quantification of phases and spheroidization in imagej

2.3 Experimental Work

This section discusses the experimental parameters used in this study. The experimental setup and specimen geometry and variations in the study experimental work is also discussed in this section.

2.3.1 Deformation Parameters

The deformation is introduced in the sample in the form of compression. The rail and wheel undergo different types of stresses depending on the position of the rail and the wheel. Such complex loading conditions is difficult to be simulated with the Gleeble1500. In the current thesis, we apply only the compressive loading due to the easier control than applying torsion, for which other cases like slip can happen. The validation for such simplification is that the major aim of the current thesis is to gain insight into the role of plastic deformation on the pearlite to austenite transformation together with heating i.e. the WEL formation.

The testing parameters are based on the work of Mr. Naeimi et al, [44] and by Jun Wu et al, [20] which simulate WEL formation via phase transformation due to temperature increase. In the current thesis, the work in [20] was extended and the role of plastic deformation was explored. The strain was adopted from Fig. 2.16 is used to study the combined effect of strain on the effective length of the specimen (20mm) at maximum 3% from the figure. This provides a maximum strain of -0.6 which is later used to program the thermo-mechanical simulator (GLEEBLE 1500) to plastically deform the sample which mimics the situation which is faced by the rail and wheel at point contact.

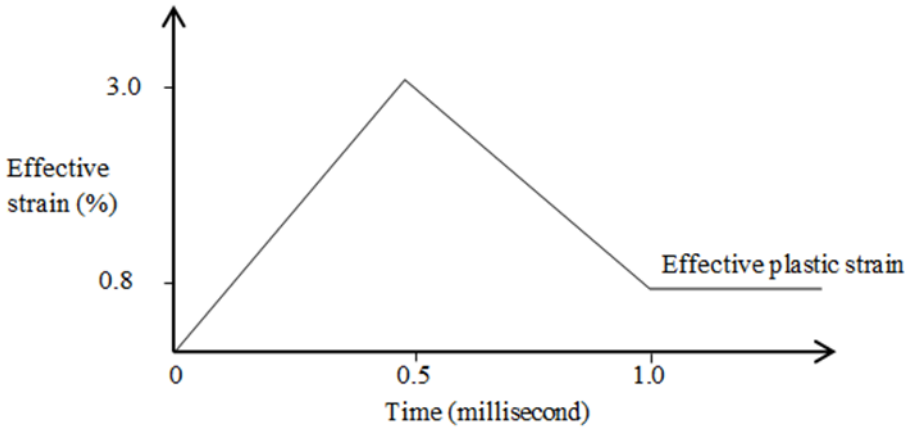

Fig. 2.16: Simplified thermo-mechanical stress-strain inputs during one contact cycle [44]

2.3.2 Experimental Setup

The experiments were done on cylindrical samples which were machined from the bottom of the rail head which is shown by the encircled region in Fig. 2.17. This region of the rail was chosen to machine the specimens as it would have the similar material composition as the head of the rail and is safe from the frictional and pressure effects on the head of the rail during service.

Fig. 2.17: Example of the region from which the sample was cut for experimental study [45]

The schematic diagram of the specimens used in the thermo-mechanical simulator is shown below.

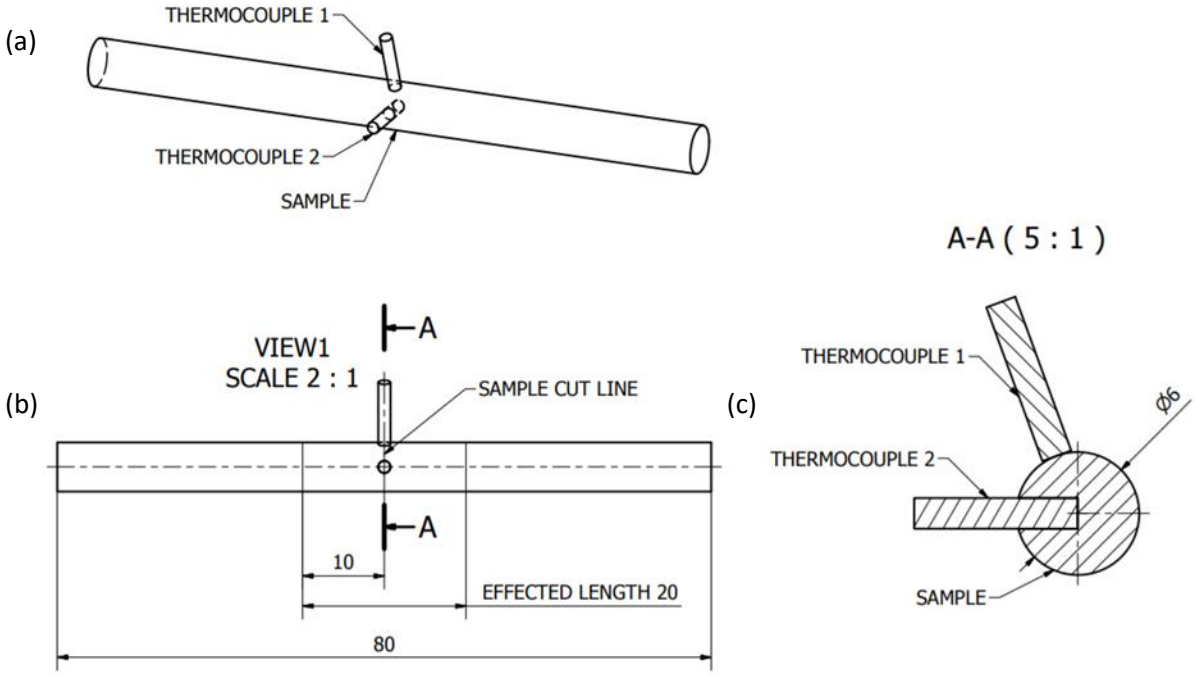

Fig. 2.18: (a) 3D view of the sample (b) 2D view (c) cross-section of the sample at the cut line

The samples were machined using the Electrical Discharge Machining (EDM) wire cutting method. The samples for simulation have a diameter of 6mm, length of 80mm and the effective length is about 20 mm (Fig. 2.19a) which is the portion in the span of the sample which undergoes various processes explained further in this section. The samples are processed in the thermo-mechanical simulator where the samples are tightly secured between two clamps which are visible in the Fig. 2.19. The picture shows the effective length of the sample on which heat and mechanical treatments are done in vacuum atmosphere. The image also shows the cooling pipe from which Helium gas with a pressure of 8 bar is let out when the sample is quenched.

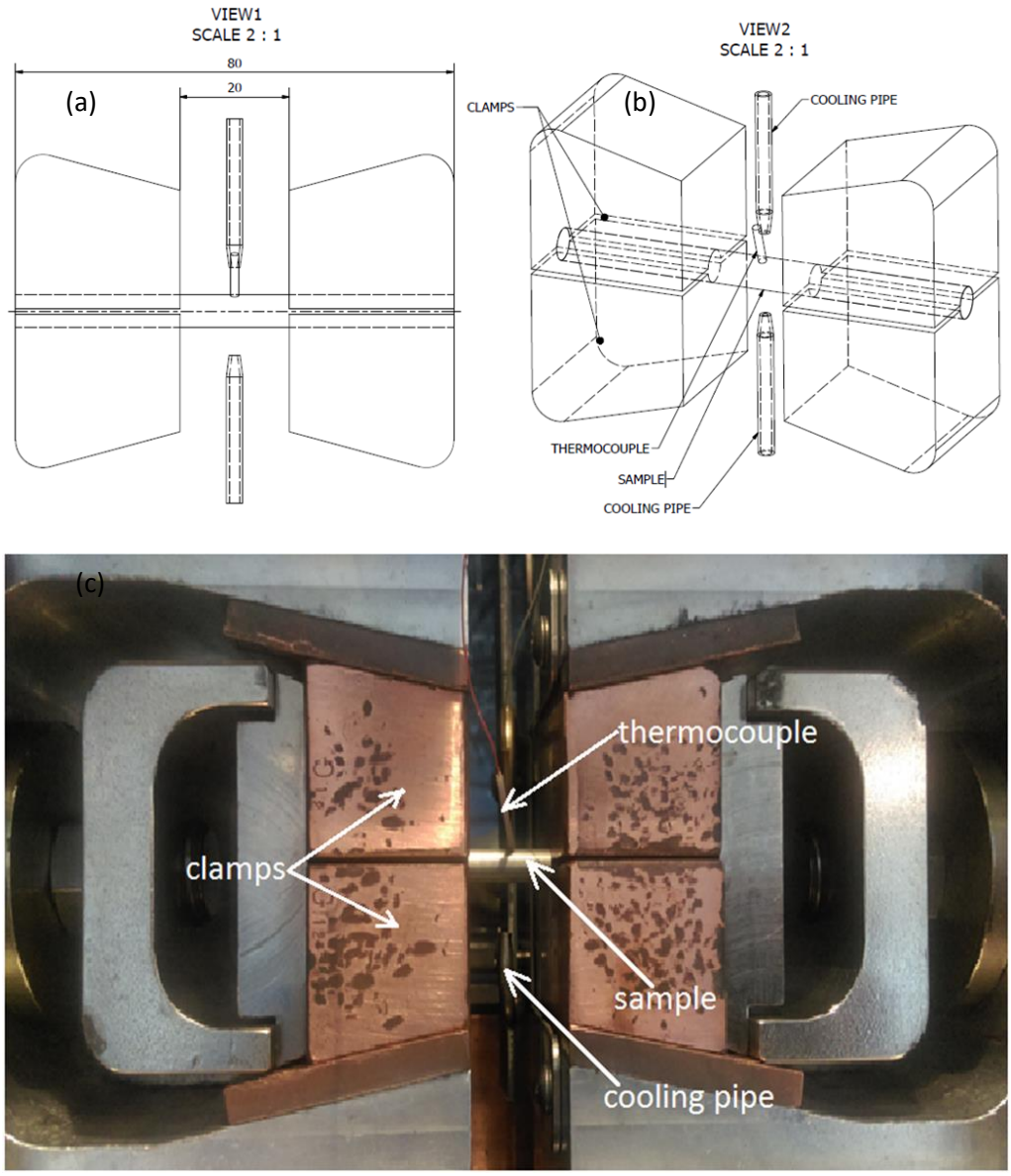

Fig. 2.19: (a) 2D view and (b) 3D view of the experimental setup (c) Photograph of the Gleeble1500 setup

The Fig. 2.20a shows the magnified image of the sample with the thermocouple connected at the middle of the longitudinal length of the sample, the sample fitted with the double thermocouples is shown in Fig. 2.20b. The ends of the sample fit between the clamps.

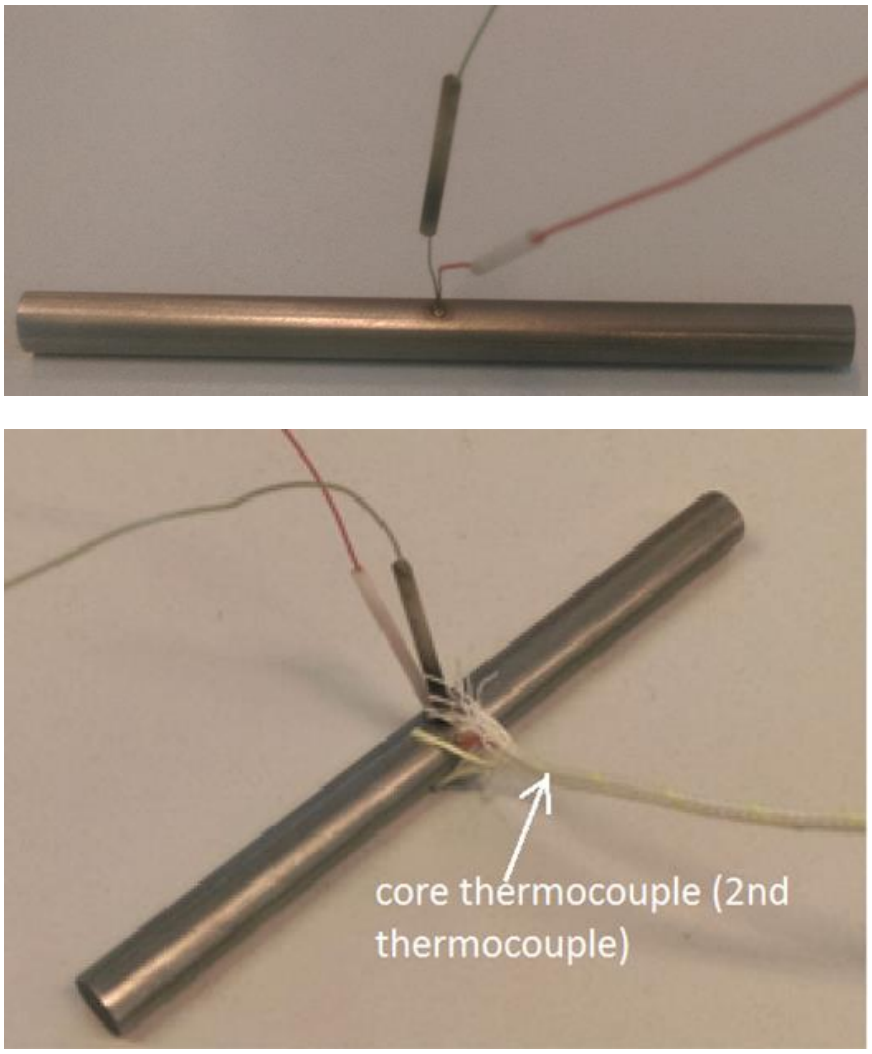

Fig. 2.20 (a) Image of sample with single thermocouple (b) Image of sample with double thermocouple

Once the sample is fitted and the Gleeble chamber closed the sample is heated from room temperature 20°C to different austenizing temperatures (T) which varies from a range of 700°C to 930°C with a heating rate of 200°C/s and is simultaneously strained from one side. After the sample reaches the maximum temperature the sample is quenched by Helium gas at 66°C/s to room temperature and this cooling rate is proven to be enough to transform the formed austenite to martensite. This process is shown in the Fig. 2.21 below:

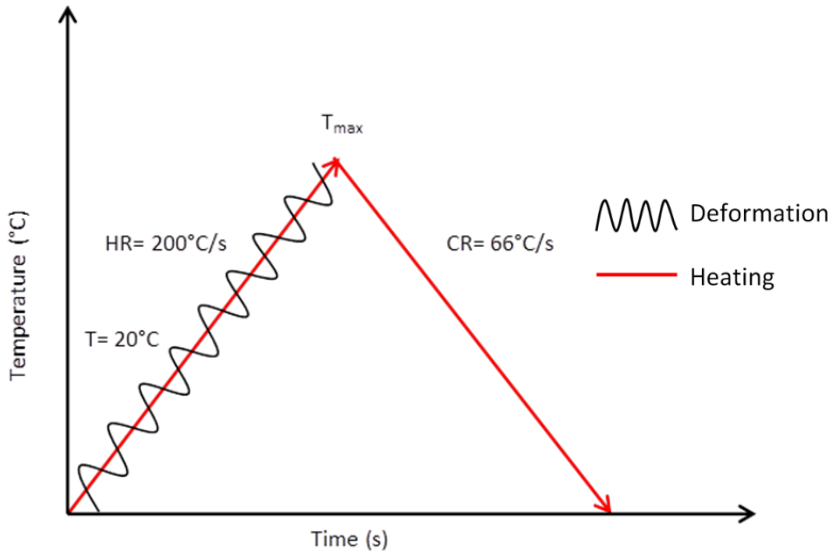

Fig. 2.21 Thermo-mechanical simulation process of single cycle

One complete process of heating and cooling is termed as one cycle and if twice heating, straining and quenching processes are done then they are considered to be 2 cycles. This procedure is to study and reproduce the process of WEL formation after multiple wheel passages. A schematic representation of the five cycle simulation is shown in Fig. 2.22 below. Another set of experiments were done where a second thermocouple was attached into the core of the sample by a hole drilled in the middle of the sample, to study the radial temperature distributions in the sample cross-section. This second thermocouple is shown in Fig. 2.20b.

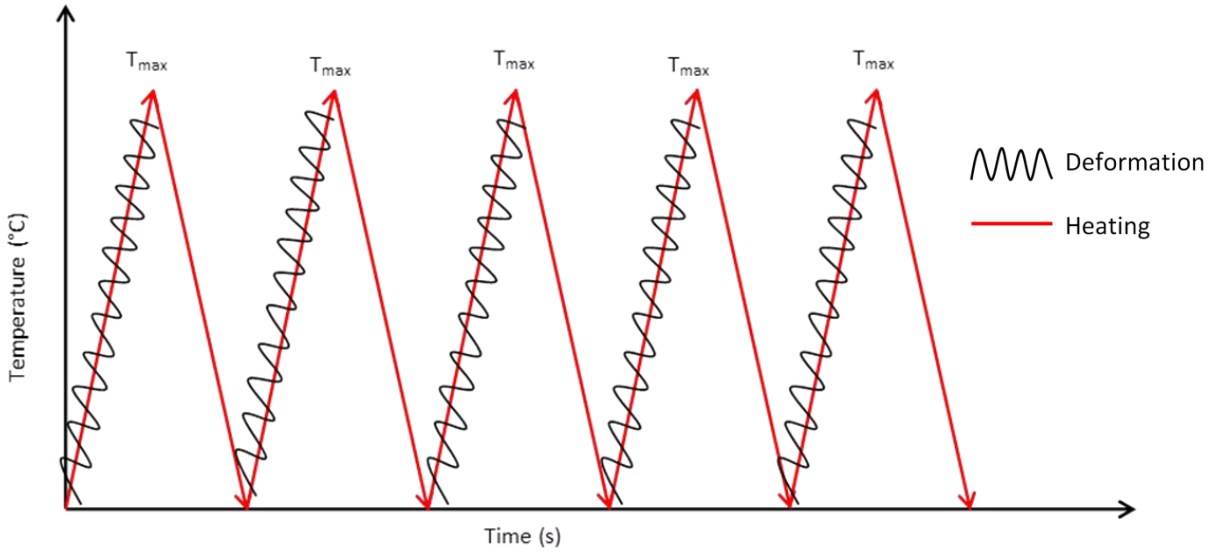

Fig. 2.22 Thermo-mechanical simulation process of five cycles

The table1 shows the samples which were processed only by heating and samples which were simultaneously heated and deformed. This is specified in the processing method column. The cycles indicate all the different cycles that were performed with different samples at the same temperature with same heating and cooling rate.

Table 2: List of the samples processed in the Gleeble and their processing methods

S.No	Sample Temperature(°C)	Processing method	Cycle
1	650	Only heating	1
2	700	Only Heating	1
3	700	Heating and deformation	1 and 5
4	730	Heating and deformation	1,3 and 5
5	830	Heating and deformation	1
6	930	Heating and deformation	1 and 5
7	700	Heating and deformation (with two thermocouples)	1

CHAPTER 3: RESULTS AND DISCUSSION

3.1 Introduction

This chapter describes the simulation of the WEL formation via martensite transformation by combined temperature increase and simultaneous deformation. The specimens were heated to temperatures ranging from 700°C to 930°C and deformed simultaneously with 3% effective plastic strain and quenched with helium to form the white featureless microstructure. The microstructures after the tests are characterized compared with the base material microstructure. Throughout the chapter the samples will be termed as "$X_{mmm\text{-}n}$" where "X" refers to the simulated sample, the symbols "mmm" refer to the maximum temperature (°C) at which the sample was processed and the symbol "n" refers to the cycles at which the sample was simulated in the Gleeble and the sample processed without strain is denoted as "$X_{mmm\text{-}nNS}$".

3.2 Microstructure of the base material

The base material microstructure of the material R260Mn before performing the experimental tests is shown in Fig. 3.1. The specimen was directly extracted from the region where the samples for simulation were cut and is considered to be free from deformation caused by the passage of rail wheels. The studied R260Mn grade rail steel has a near eutectoid carbon concentration of about 0.67wt% and a fully pearlitic microstructure is characterized.

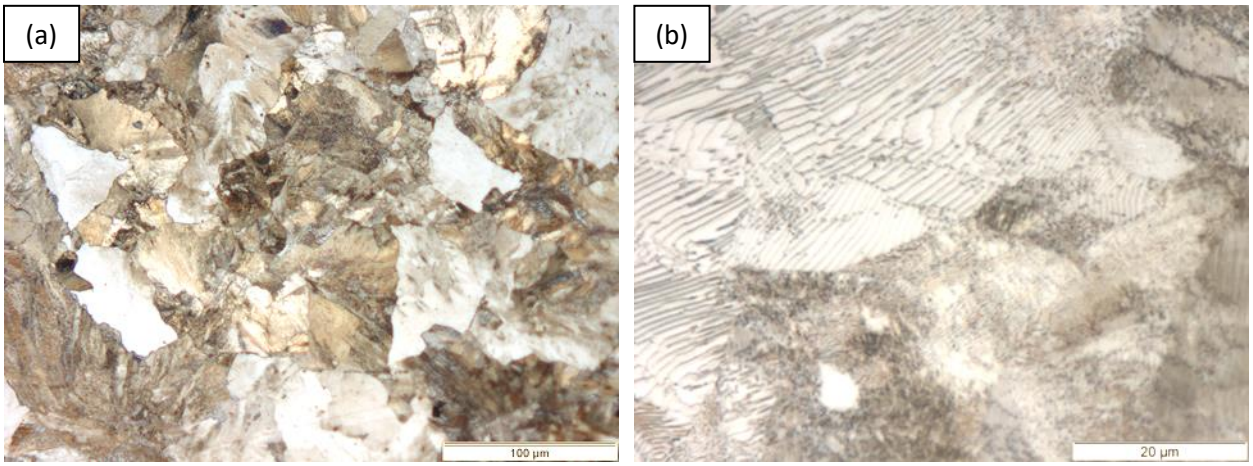

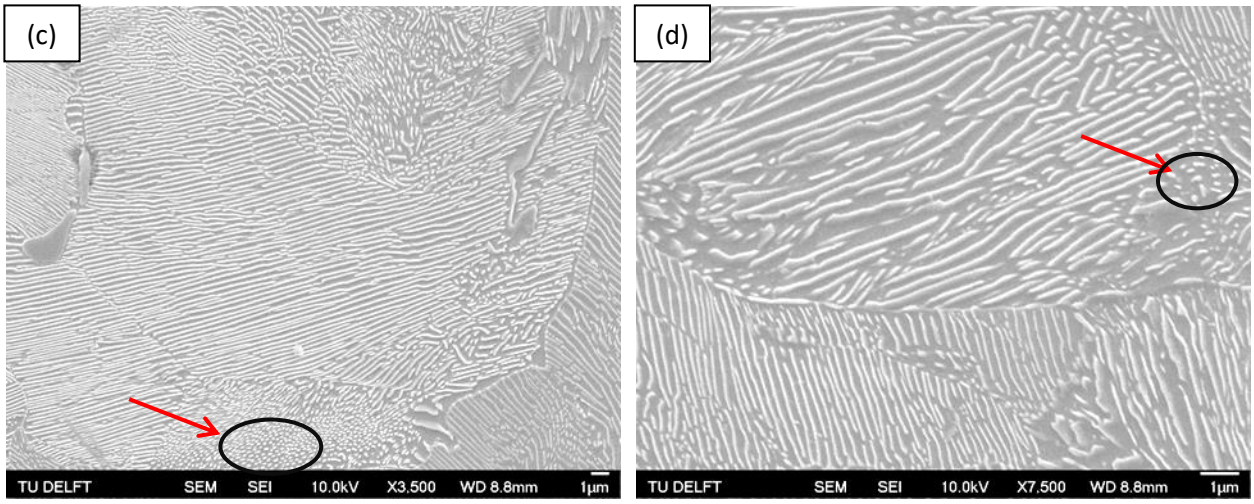

Fig. 3.1 OM and SEM images of reference (a) (c) low magnification (b) (d) high magnification

Fig.3.1 a, b show the OM images of the reference pearlite at low and high magnification respectively. In the lower magnification image (Fig.. 3.1a) pearlite can be seen to be present as both dark and light regions due to the differences in response to the etching of the pearlite colony orientation. The higher magnification image shows the lamellar structure of the pearlite which can also be seen in Fig. 3.1 (c) and (d) at different magnifications. The interlamellar distance in the base material is about 150nm [20]. The arrow indicates the regions where the pearlite structure is seen to be broken to small spherical shape like structures called spheroids which are present in pearlite as a sign of deformation. This could have occurred due the various manufacturing processes of the base material.

3.3 Microstructure of the simulated WEL

This section discusses the results obtained from the optical microscopy and the scanning electron microscope analysis of the thermo-mechanically simulated samples. The samples were tested at various temperatures from 650°C to 930°C and the important results on the WEL simulation are discussed in this section. The samples after the thermo-mechanical process were cut to reveal the cross-section at the position where the thermocouple is placed. Fig. 3.2 shows an example of the cross-section of sample $X_{700\text{-}1}$ to help in understanding the cross-sections. From Fig. 3.2 a difference in certain areas (dark and light) of the region highlighted in red noticed in this sample is not always exactly seen in the other samples. All the samples discussed in the future sections will be referred to as (i) middle region (middle area which is not highlighted in Fig. 3.2) and (ii) near surface region (highlighted region).

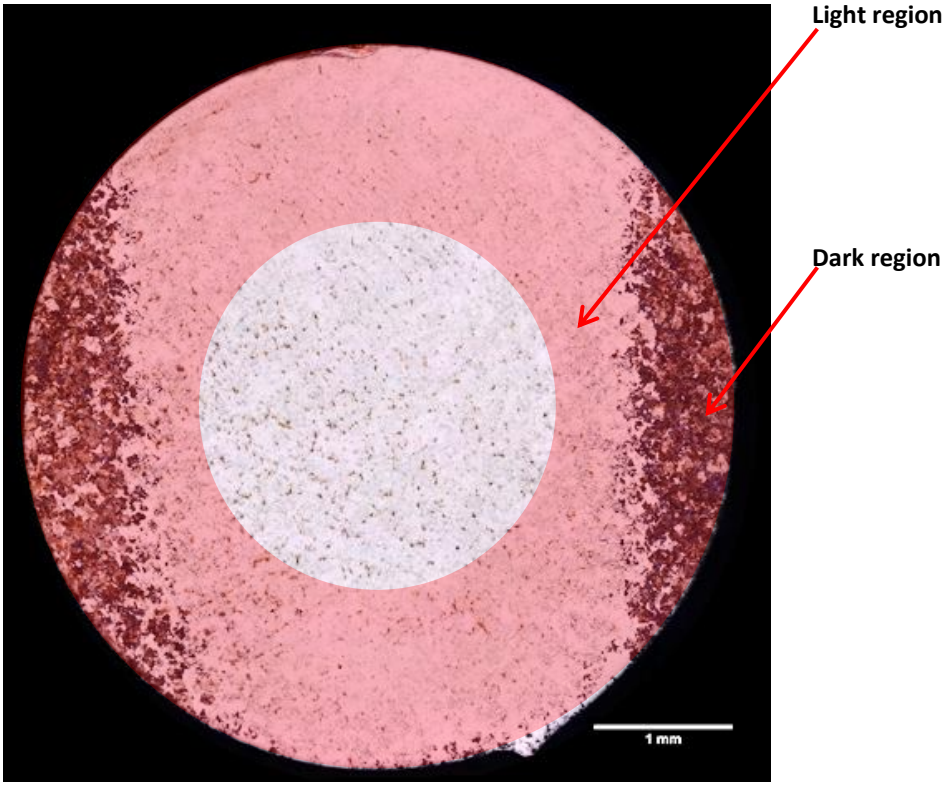

Fig. 3.2 Cross-sectional OM image of the sample X_{700}

3.3.1 Microstructure of samples tested at 700°C (X_{700})

The samples tested at this temperature have two main parameters that have been varied during the simulation such as strain and number of simulation cycles. The sample $X_{700\text{-}1NS}$ is the sample where WEL was simulated using heating followed by quenching. Fig. 3.3 (a-d) shows the optical and SEM images of the simulated WEL in sample $X_{700\text{-}1NS}$. Fig. 3.3a shows the OM image with the white islands, which is the simulated WEL, pointed by the arrows. The WEL can be differentiated from the surrounding pearlite which can also be light. At higher magnifications difference can be spotted in the light phases between the WEL and pearlite. The ferrite- cementite lamellae can be noticed in the pearlite blocks indicated by the black arrow in Fig.. 3.3b, the simulated WEL is featureless even at higher magnification indicated by the red arrow (1) in the same figure and the featureless aspect in the WEL can also be seen in the SEM image (Fig. 3.3c). The dark brown area seen in the WEL which is identified to be untransformed pearlite by using SEM shown in Fig. 3.3c indicated by the red arrow(2) in the same image. In the WEL some lamellae features are noticed indicated by arrows in Fig. 3.3c and in the magnified image of Fig. 3.3d which could be the cementite particles from the lamellae before transformation. Moreover in the magnified image of the simulated WEL aligned lamellae like features can be seen (Fig. 3.3d). They are consistent in the WEL and could probably be the previous location of the cementite lamellae.

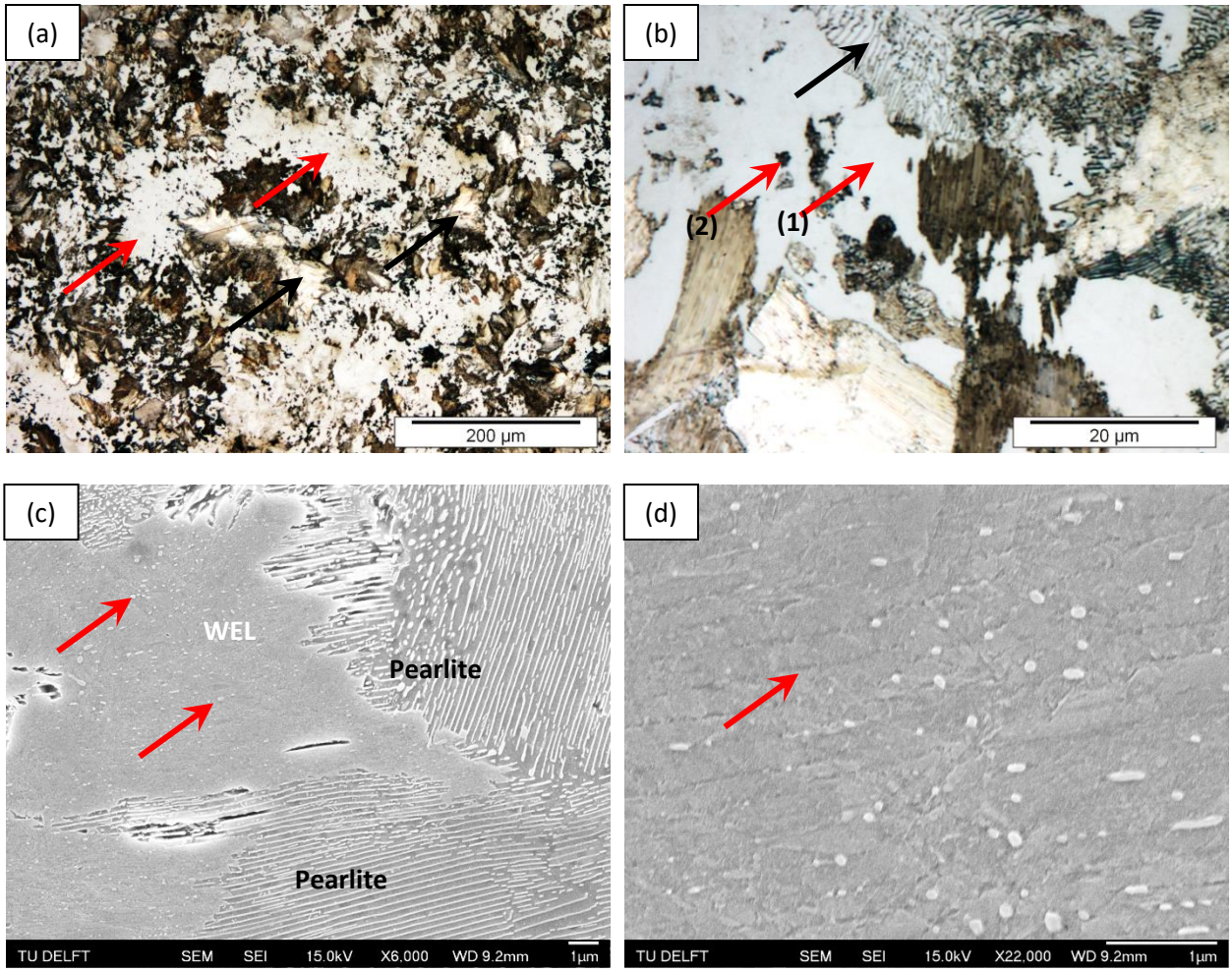

Fig: 3.3 Optical and SEM images of sample processed at 700°C without strain (X700-1NS) (a) WEL at100x (b) WEL at 500x (c) SEM of feature in WEL WEL (d) Aligned

Figure 3.4 (a-d) shows the Optical micrograph and SEM images of sample $X_{700\text{-}1}$ which is also deformed. Untransformed pearlite can be seen in the highlighted region (fig. 3.2) is shown in fig. 3.4 and the SEM image of the pearlite is shown in fig. 3.4c. The amount of simulated WEL is higher (fig. 3.4b) in this sample and more homogenous than compared to the sample $X_{700\text{-}1NS}$.This is due to the simulation of WEL using strain as all other parameters during the simulation process of samples $X_{700\text{-}1NS}$ and $X_{700\text{-}1}$ is the same excluding strain. Brown spots are seen in the light phase indicated by arrows in fig. 3.4b. As mentioned in the previous page, these brown spots could be small untransformed pearlite regions which can be noticed at higher magnification in SEM (Fig.3.4d). Accordingly the white blocks will be considered to be martensite and the dark regions to be pearlite in the rest of the chapter. It can be also noticed that cementite lamellae (Fig. 3.4c) which seems to be broken into fragments shown with black arrows (Fig. 3.4c) are seen only in certain regions which may have undegone localised strain, similar to occurrence of shear bands.

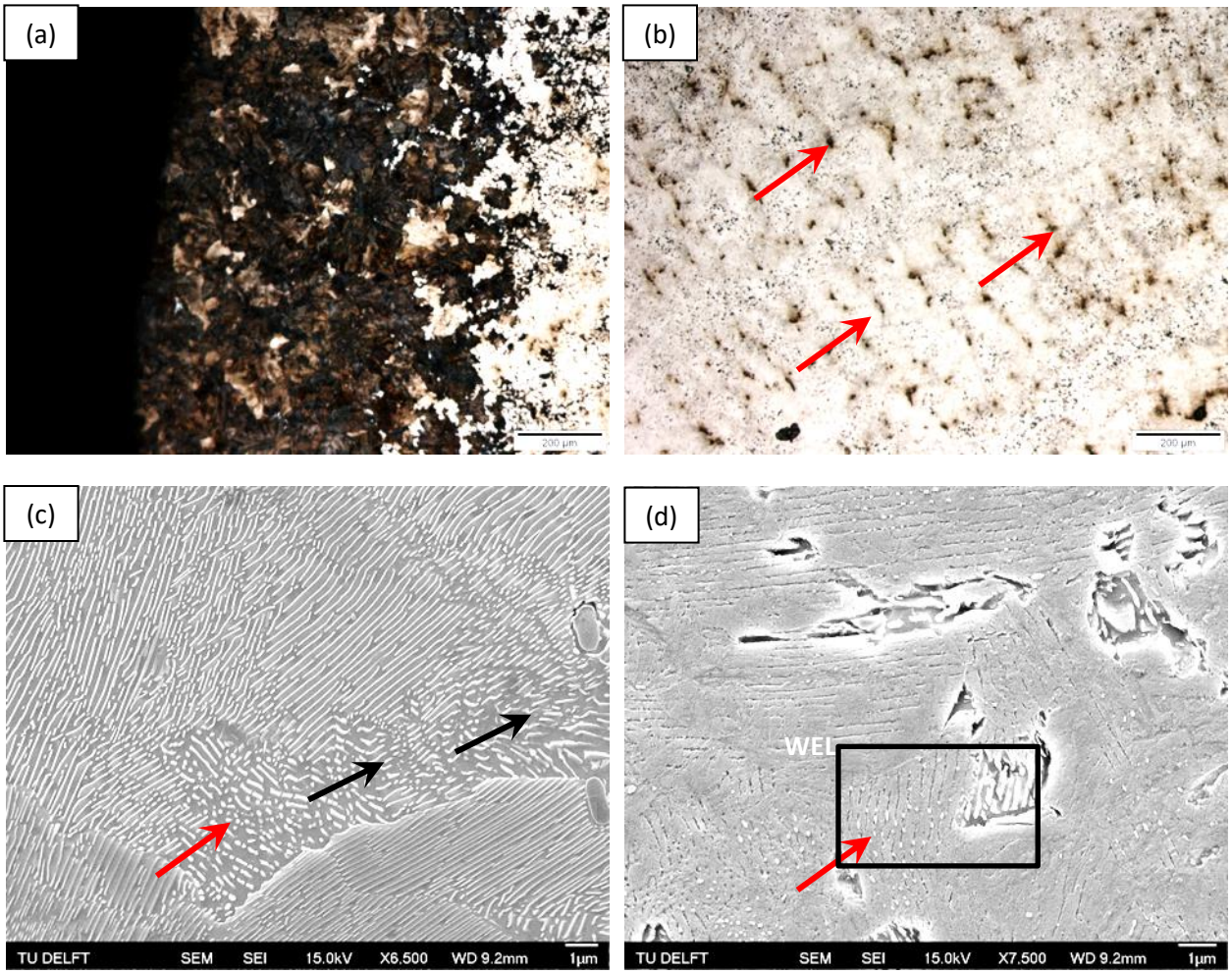

Fig. 3.4 Optical and SEM images of simulated WEL processed at 700°C with strain ($X_{700\text{-}1}$) (a) $X_{700\text{-}1}$ (50x, highlighted region) (b) $X_{700\text{-}1}$ (50x, middle region) (c) SEM of pearlite (d) SEM of WEL

The WEL in the sample $X_{700\text{-}1}$ has aligned features similar to the simulated WEL as discussed in [20] which can be seen in Fig. 3.4d indicated by the arrow. The distance between the lamellae features in the WEL and cementite lamellae adjacent to it is very similar which indicates the relation with the cementite lamellae before it had transformed. Also small particles seem to occupy the lamellae of the WEL at the location in the area inside the rectangle in fig. 3.4d. These are similar to the broken cementite particles which can be seen in Fig. 3.3c, indicated by the red arrow, which provides more evidence to consider them as cementite locations before WEL was formed. Optical and SEM images of sample $X_{700\text{-}5}$ are shown in Fig. 3.5. The simulated WEL region formed by continuous cyclic thermo-mechanical simulation is more homogenous (Fig. 3.5b) than compared to the sample $X_{700\text{-}1}$ (Fig. 3.4b). The brownish spots indicated by the arrows in Fig. 3.5b shows untransformed cementite islands as seen in the previous images but these are finer than other images of samples processed at 700^{o}C.

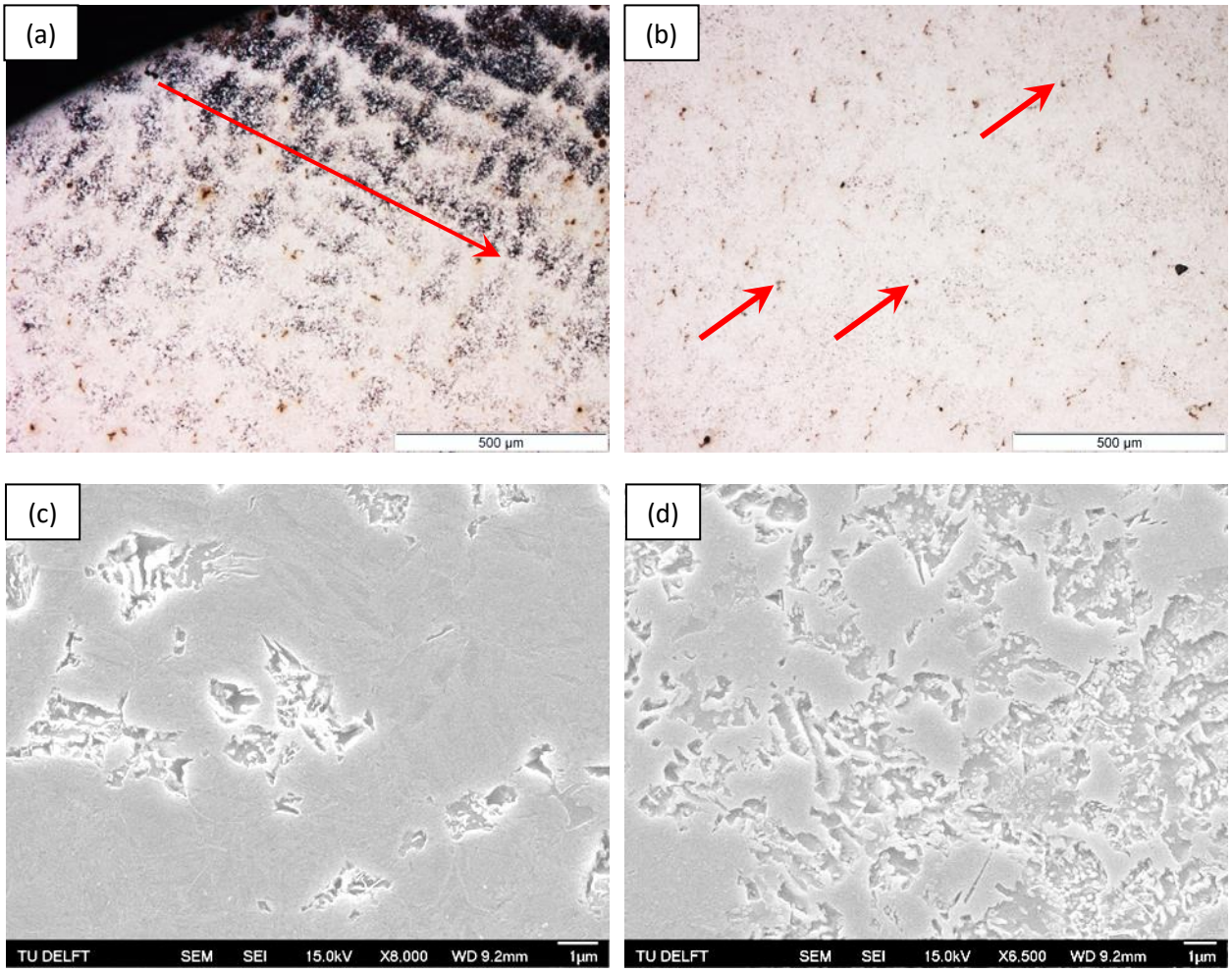

Fig. 3.5 Optical micrographs of simulated WEL processed at 700°C ($X_{700\text{-}5}$) (a) (50x, corner region) (b) $X_{700\text{-}1}$ (50x, middle region) (c) $X_{700\text{-}5}$ (50x, corner region) (d) $X_{700\text{-}5}$ (50x, center region)

It can be noticed that as the number of cycles increase the amount of WEL formed at 700°C and the SEM image of the WEL in Fig. 3.5c also does not show any aligned lamellae features as discussed in Fig.3.4d. The WEL seems to have multi-directional features similar to the features found in the WEL normally formed in the rail which has been discussed in [20]. Certain band like structures can be noticed in the near surface region of the sample shown in Fig. 3.5a. The dark regions correspond to the pearlite areas and the light areas close to the banding regions can be identified as WEL from the SEM image (Fig. 3.5d). The cementite lamellae shown in the same figure are seen to be broken heavily that the lamellae structure is lost.

3.3.2 Microstructure of samples tested at 730°C (X_{730})

The samples were tested at one, three and five cycles at this temperature and are denoted as " $X_{730\text{-}1}$, $X_{730\text{-}3}$, $X_{730\text{-}5}$". An important feature witnessed in the simulated WEL at the 730°C is the

band features that can be seen in the samples at all cycles shown in Fig. 3.6 (a-f). Though the band like feature is witnessed only in sample $X_{700\text{-}5}$ in the highlighted region (Fig. 3.5a), the banding features observed in X_{730} samples can be seen in Fig. 3.6 in all areas of the samples.

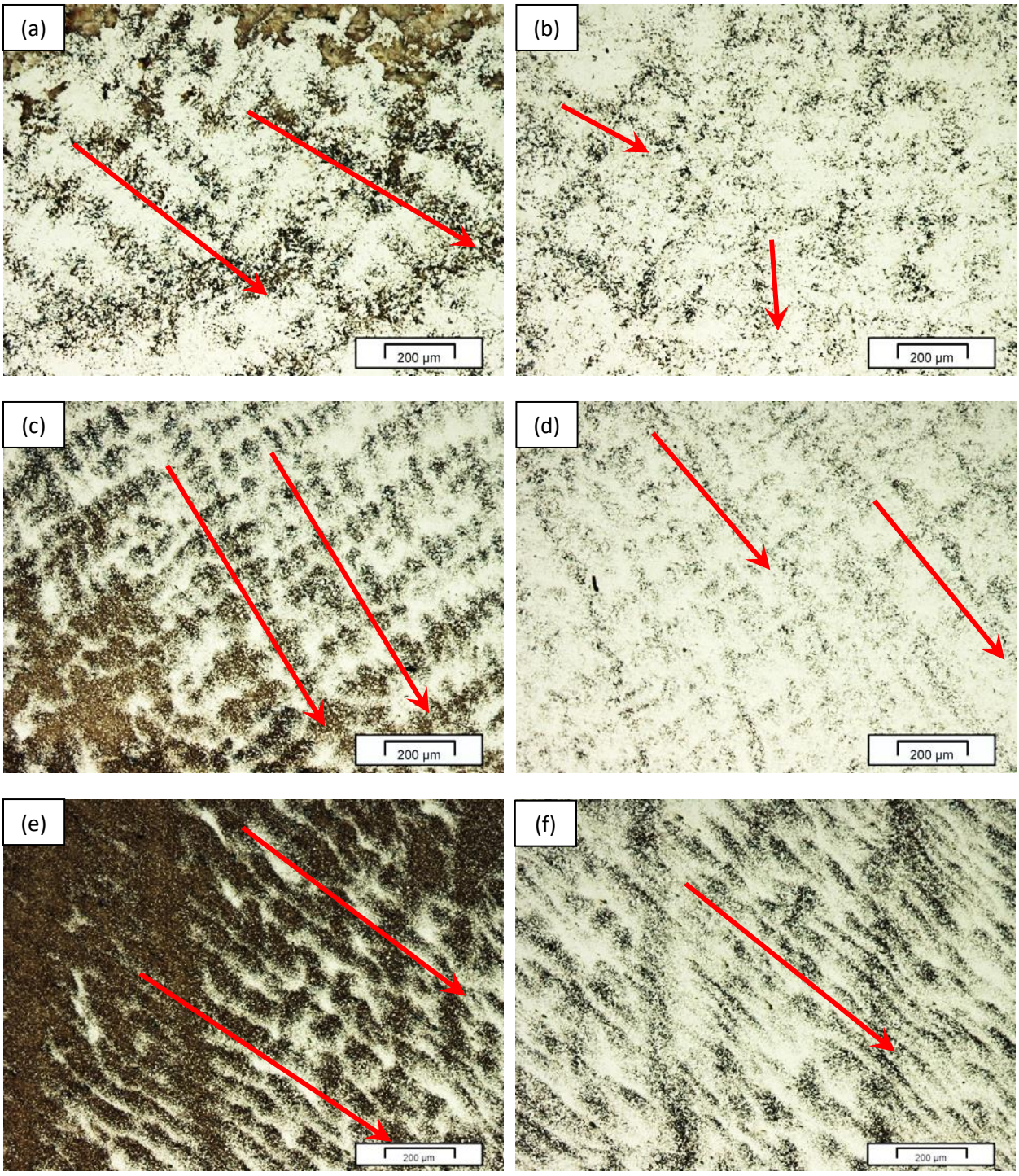

Fig. 3.6 OM images of simulated WEL processed at 730°C (X_{730}) (a) (c) (e) banding structures in $X_{730\text{-}1}$, $X_{730\text{-}3}$ and $X_{730\text{-}5}$ at highlighted region at 100x (b) (d) (f) corner region at 100x

It can be spotted that the banding in sample $X_{730\text{-}1}$ has light and random bands in the near surface region (Fig. 3.6a) and the middle region of the sample has less pronounced bands t the near surface region. This pattern can also be spotted in the OM images of the samples $X_{730\text{-}3}$ and $X_{730\text{-}5}$ (Fig. 3.6 c-f) but in these samples, the banding feature seems to become more pronounced also in the middle region of the sample as seen in Fig. 3.6 d and f. Firstly to know about the WEL region formed and the structure of the band areas the SEM images of the samples X_{730} are studied. The lower magnification image (Fig. 3.7a) shows the band type feature similar to the feature seen in the OM images and at higher magnification (Fig. 3.7b) of the selected rectangle area shows islands of featureless martensite region (WEL) surrounded by pearlite regions. The pearlite regions in the X_{730} samples are seen to have many areas where the cementite lamellae are fragmented to small pieces (Fig. 3.7c) and many spherical cementite particles as a result of the breaking of the lamellae are also seen in the magnified image in sample $X_{730\text{-}5}$ indicated by arrows in Fig. 3.7d.

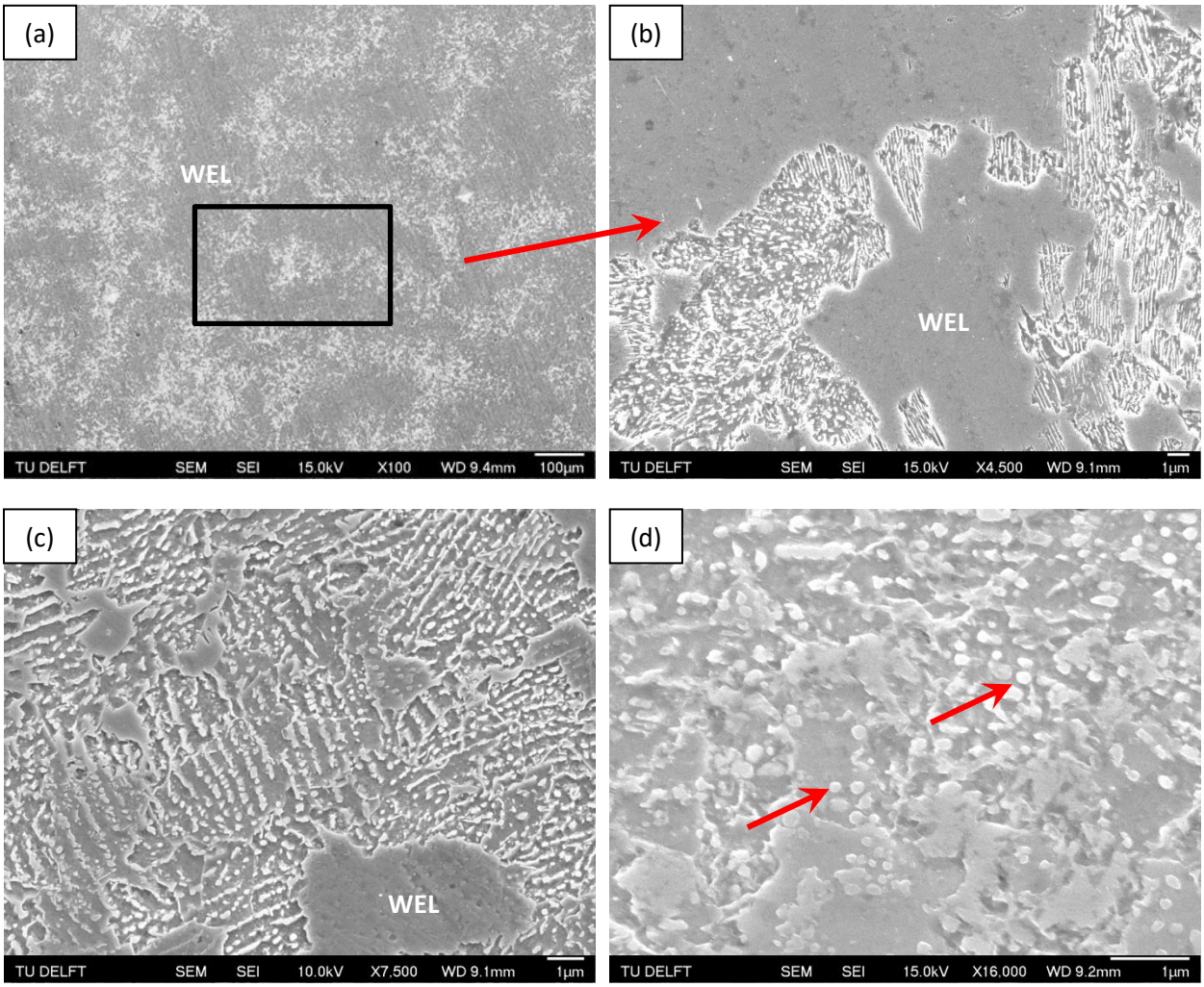

Fig: 3.7 SEM images of simulated WEL processed at 730°C (X_{730}) (a) (b) WEL in $X_{730\text{-}1}$ (c) WEL in $X_{730\text{-}3}$ (c) cementite in $X_{730\text{-}5}$

Results of the sample X_{730} from a previous set of thermo-mechanical simulations suspected to be flawed are shown in figure 3.8(a and c) only for comparison purposes. This set of samples will be referred to as "$X_{mmm\text{-}nold}$" in this chapter. Digital microscopy cross-sectional images of samples ($X_{730\text{-}3old}$ and $X_{730\text{-}3}$) and ($X_{730\text{-}5old}$ and $X_{730\text{-}5}$) are compared to analyze the banding structure that is present heavily in samples processed at 730°C. Though $X_{730\text{-}3old}$ and $X_{730\text{-}3}$ have been simulated with the same parameters, in $X_{730\text{-}3old}$ greater level of pearlite can be noticed indicated by arrows than $X_{730\text{-}3}$ and in $X_{730\text{-}5old}$ higher level of martensite (light regions) can be seen than compared to $X_{730\text{-}5}$. Dissimilarity can also be seen in the intensity of the banding structure which can be easily noticed between the samples $X_{730\text{-}5old}$ and $X_{730\text{-}5}$.

Theoritically it can be assumed that the sample undergoing thermo-mechanical simulaton just above the eutectoid temperature (727°C) at which partial transformation from pearlite to austenite and subsequently martensite during quenching can easily occur which can ensure quantitatively higher amount of martensite formation in a single cycle. It can be also assumed that when the number of simulation cycles increases the amount of martensite formed will be higher than compared to a single cycle and also will be more homogenously distributed . Though exact reproduction of results is not observed, the significant discrepencies in the results (Fig. 3.8) can be probably due to either instrumental errors that can arise during the simulation due to programmed heating, deformation and cooling cycles controlled by the machine or segregation of alloying elements on certain areas that create banded regions. This banding structure is further studied by EPMA to analyze the possibility of segregation of alloying elements along the bands.

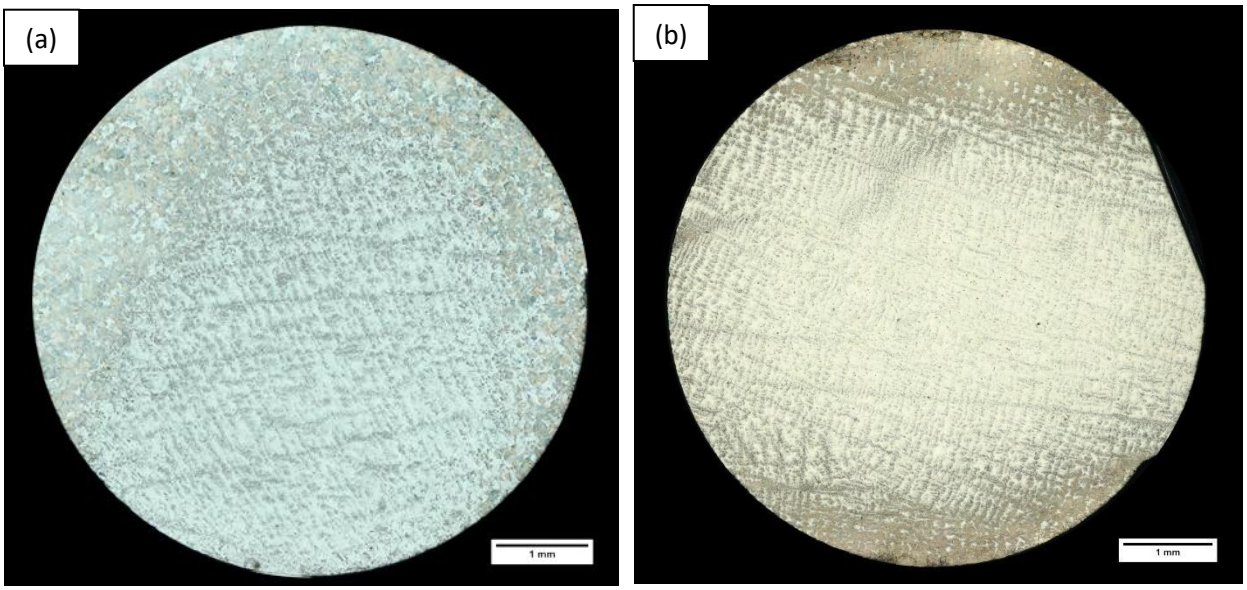

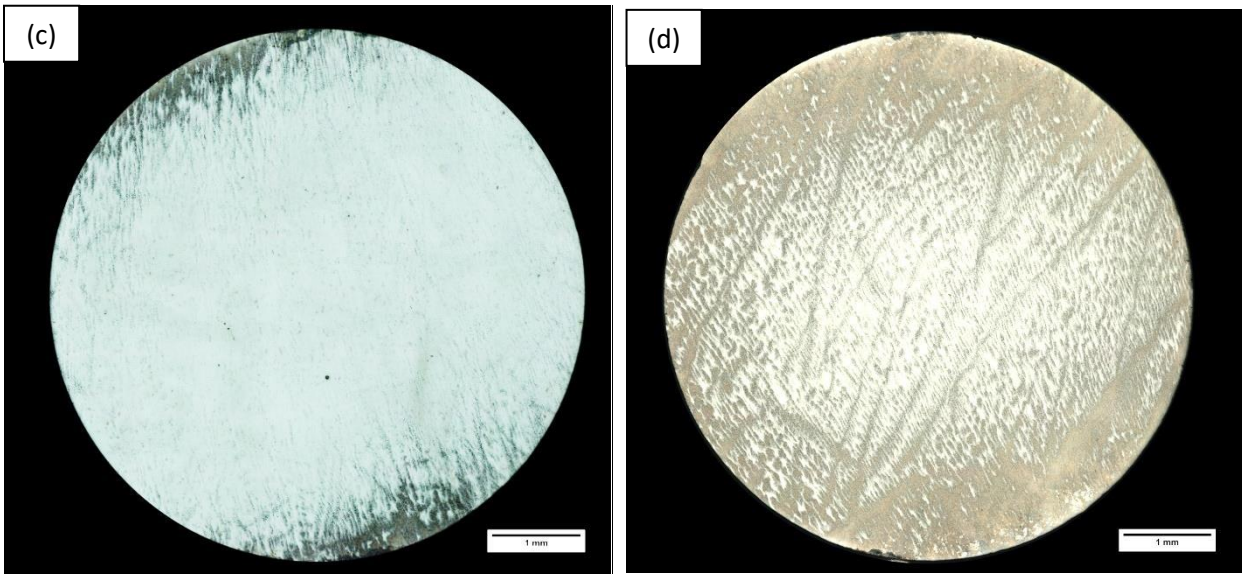

Fig: 3.8 Digital microscopy images (a) $X_{730\text{-}3old}$ (b) $X_{730\text{-}3}$ (c) $X_{730\text{-}5old}$ and (d) $X_{730\text{-}5}$

Similar banding structures are observed in literature [46] and are known to occur due to the dendritic solidification which introduces segregation of the substituitional alloying elements. Investigations have shown Manganese (Mn) to be the element mostly responsible for the banding due to the migration of carbon from low to high Mn regions. Hence secondly EPMA tests were done on the bands to know more about the presence of Mn in the bands.

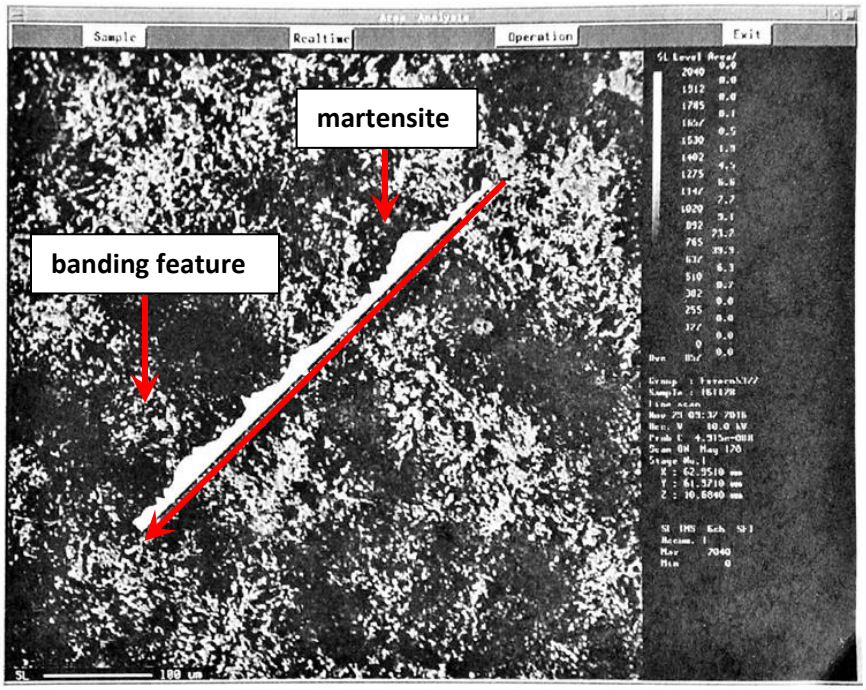

Fig: 3.9 Analysis of the line scan on the steel sample along the arrow in SEI image

Figure 3.9 shows the microstructure on which the tests were done, the area taken for the tests was along the regions indicated by the arrow ending at the arrow head which is the band structure region (light areas) seen in the optical micrographs of X_{730} sample . The area selected for the test is from one of the samples simulated at 730°C.The results from the EPMA tests are shown in Fig. 3.10. It can be observed that there is a variation in the Mn content that could cause banding but there is no severity of Mn segregation in the banded areas as high peaks of Mn content can be noticed in both banding area and the martensite area. There is no proper one to one correspondence between the Mn content and the banding feature. Hence the banding could be probably due to the instrumental errors during the simulation.

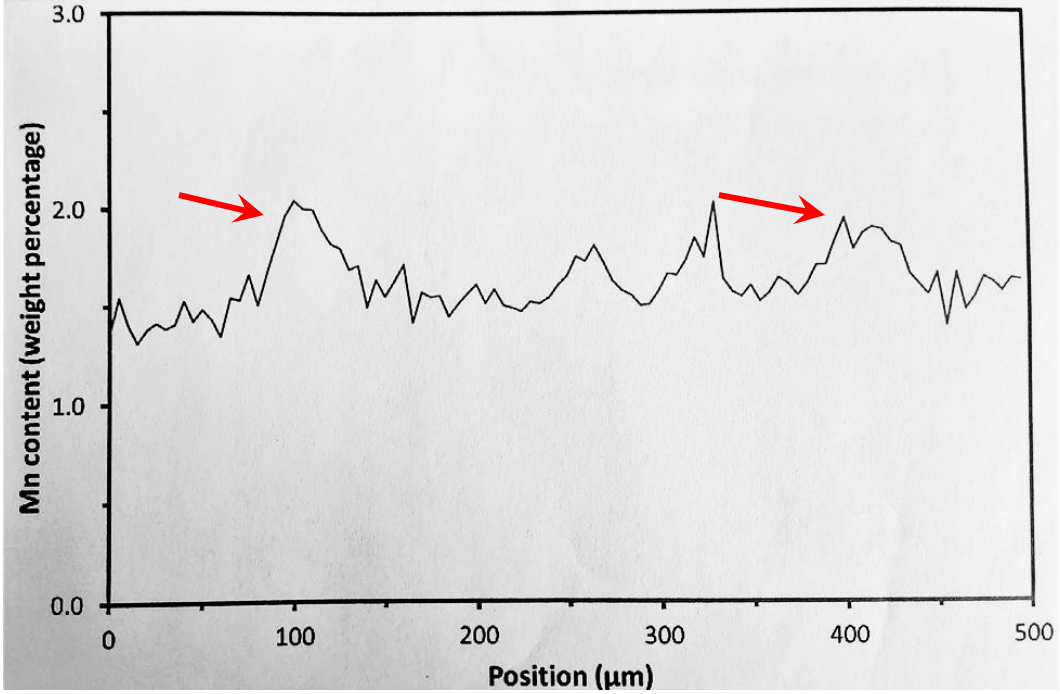

Fig. 3.10 Manganese content in weight percentage plotted for each position along the 500 µm line

3.3.3 Microstructure of samples tested at 830°C (X_{830})

The WEL simulated at 830°C is distinctly above A_1, so uniform featureless regions can be seen in the lower magnification image in Fig. 3.11a. Small dark regions observed in WEL simulated at lower temperatures can also be found in the WEL at X_{830}. No banding can be seen in the WEL and the microstructure of WEL at higher magnification shows mostly homogenous martensite features. The SEM images show multi-directional lamellar formation (Fig. 3.11c) unlike the aligned lamellar structures discussed previously. Multi-directional lamellae in the WEL can also be seen in the rail WEL studied in[20]. At higher magnification of the WEL small particles can be seen in the WEL (Fig. 3.11d) which could probably be the cementite particles from the pearlite matrix.

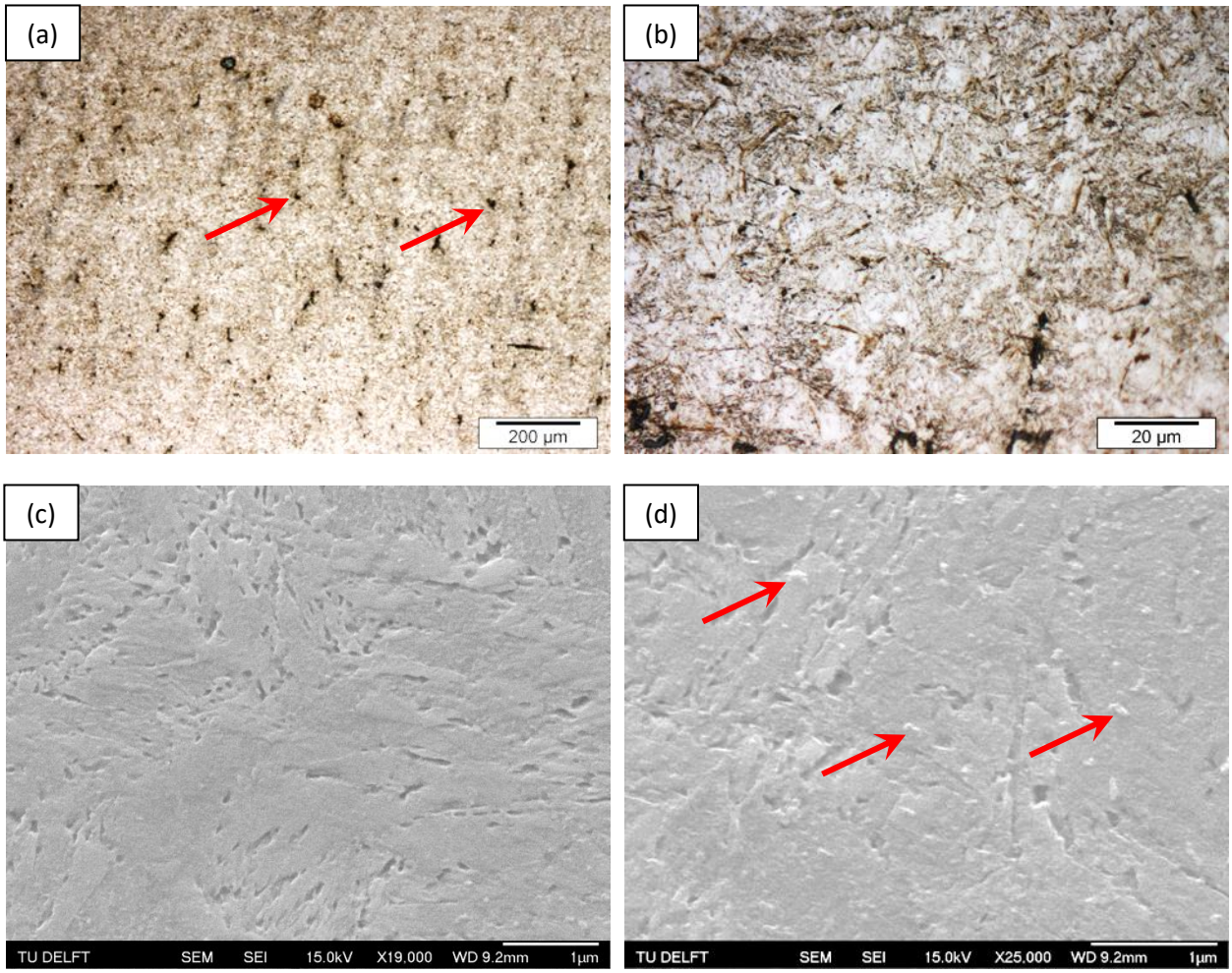

Fig: 3.11 Optical and SEM images of simulated WEL processed at 830°C ($X_{830\text{-}1}$) (a) OM of WEL (50x), (b) OM of WEL (500x) (c) SEM of WEL (d) cementite particles in WEL

3.3.4 Quantification of phases from optical microscopy images

The completeness of transformation from pearlite to austenite and subsequently to WEL (martensite) of samples simulated at different temperatures and different simulation cycles can be seen in figure 3.12. The percentage of martensite present in the 700°C samples is observed to increase as cycles increase. In the X_{700} samples the amount of martensite is noticed to increase steadily from 9% in $X_{700\text{-}1NS}$ (simulated only with a heating cycle) to 85% in $X_{700\text{-}5}$ (simulated with both heating and deformation). However in samples (X_{730}) processed close to the eutectoid transformation temperature (727°C) patterns observed in X_{700} samples are not always witnessed. Though an increase in the percentage of martensite present is seen in sample $X_{730\text{-}3}$ of about 36% as compared to $X_{730\text{-}1}$, the amount of martensite transformed decreases in $X_{730\text{-}5}$ by 21% when compared to $X_{730\text{-}3}$. When the samples with similar cycles but different temperatures ($X_{700\text{-}1}$, $X_{730\text{-}1}$, $X_{700\text{-}5}$ and $X_{730\text{-}5}$) are compared, difference observed in the percentage of martensite present in $X_{700\text{-}1}$ and $X_{730\text{-}1}$ is about 12.5% higher in $X_{700\text{-}1}$. Major

difference can be noticed of about 42% higher presence of martensite in $X_{700\text{-}5}$ compared to $X_{730\text{-}5}$ as higher percentage of untransformed pearlite is present in $X_{730\text{-}5}$ which is noticed as the banding strucutres in (Fig. 3.6f) than compared to $X_{700\text{-}5}$ (Fig. 3.5c). Simulation of WEL at higher temperature shows the highest percentage of martensite formed of about 95%.

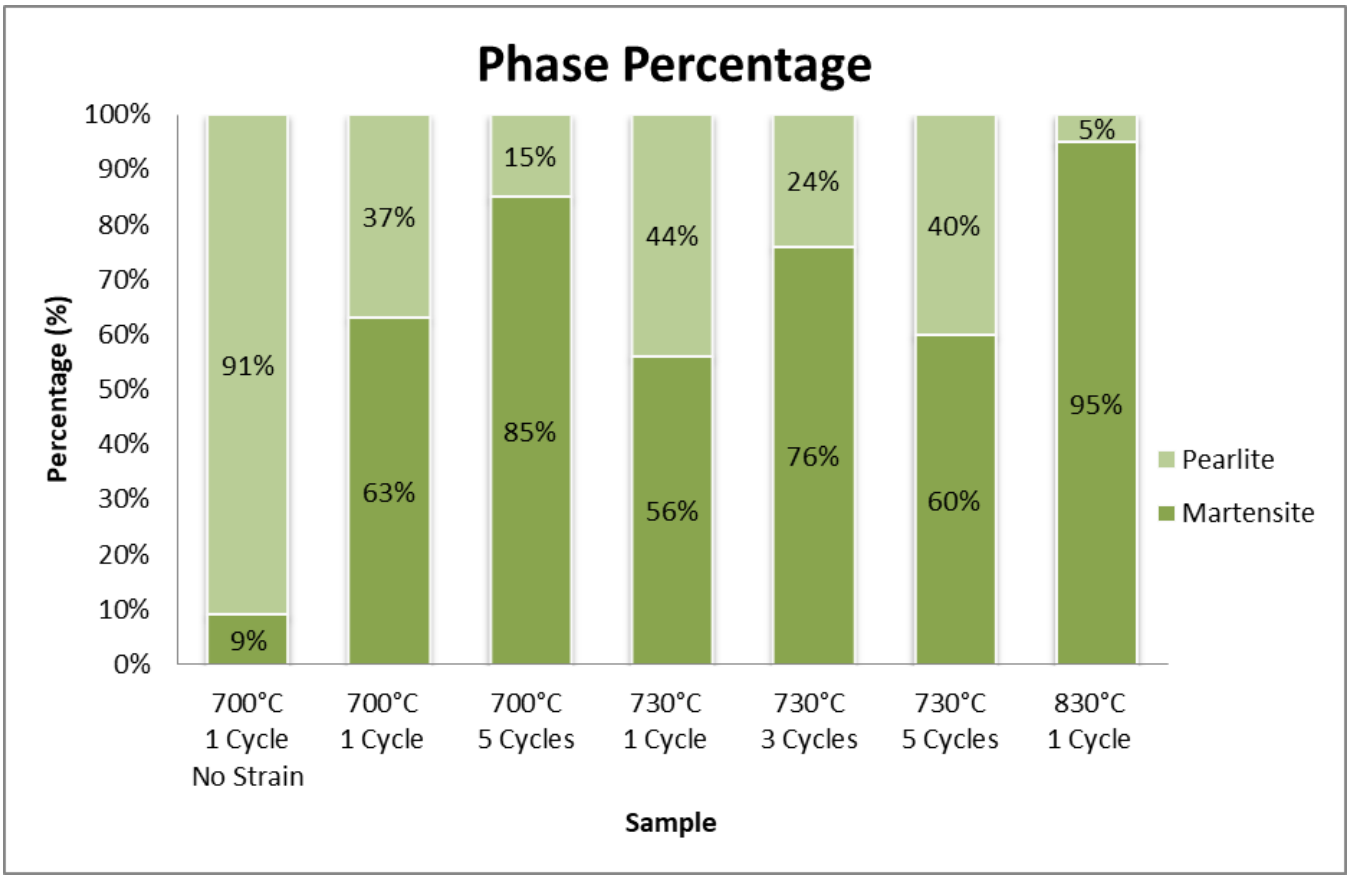

Fig: 3.12 Percentage of Marternsite and Pearlite phases formed in the samples

3.4 Hardness Results

Hardness is tested in the dark and light phases observed in the simulated samples , examples of these phases are seen in figure 3.13. The indents that occur from the diamond indenter of the vickers micro-hardness can be seen in the same figure. The indents are carefully made on the respective areas which are tested to obtain accurate results and reduce any error that can arise while hardness measurement.

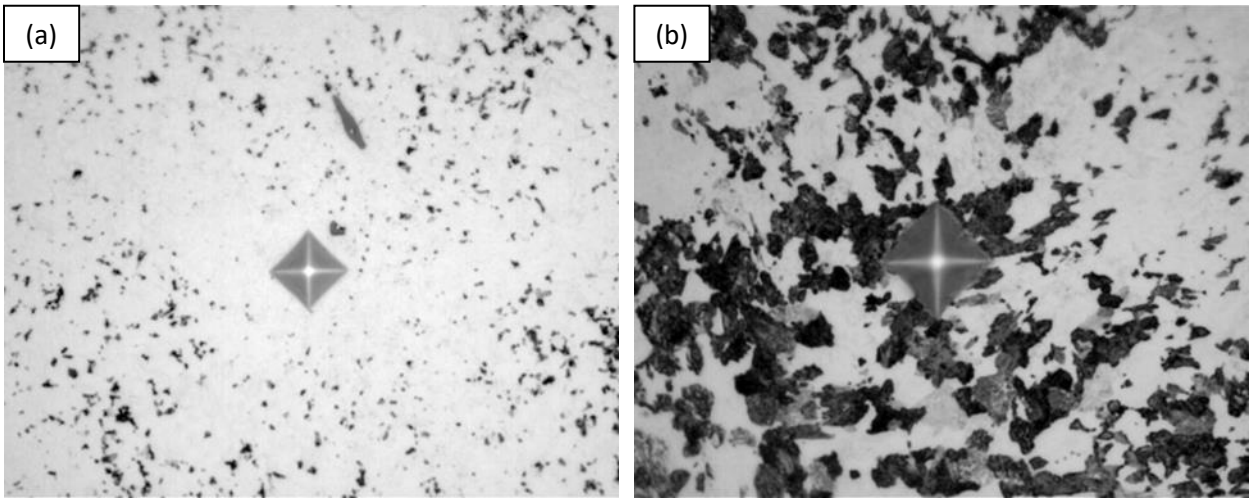

Fig: 3.13 Example of the areas tested for hardness (a) Light phase (WEL) 40x (b) Dark phase (untransformed pearlite) 40x

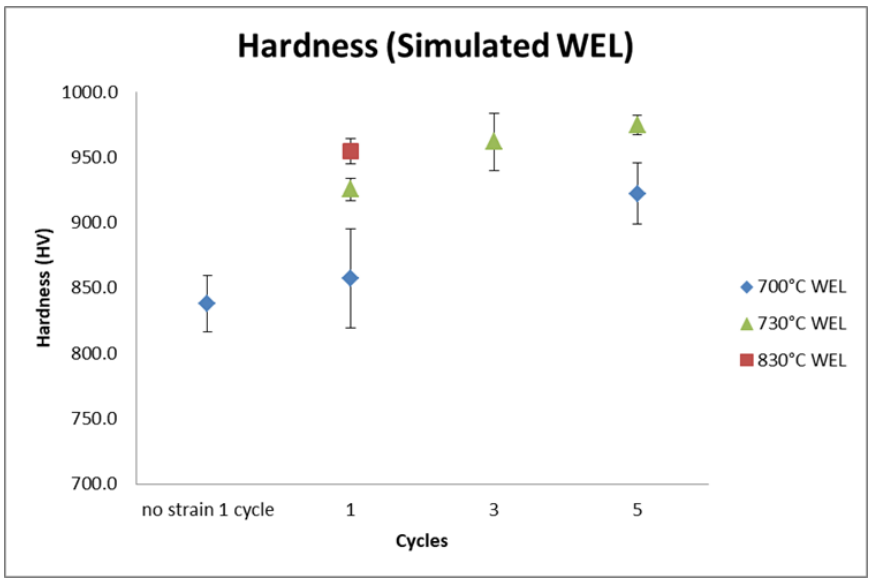

Fig: 3.14 Hardness of simulated WEL

The hardness of the simulated WEL and untransformed pearlite at different temperatures and simulation cycles are seen in Fig. 3.14 and Fig. 3.15. Hardness of WEL is noted to increase with temperature and cycles in X_{700} and X_{730} samples. WEL hardness in $X_{700\text{-}1NS}$, $X_{700\text{-}1}$, $X_{700\text{-}5}$ is approximately about 840HV, 860HV and 920HV respectively and hardness of WEL in $X_{730\text{-}1}$, $X_{730\text{-}3}$ and $X_{730\text{-}5}$ is about 925HV, 960HV and 975HV respectively. It can be noticed that only a 2.4% increase in hardness is found in $X_{700\text{-}1}$ when compared to $X_{700\text{-}1NS}$ which is inconclusive to determine the effects of deformation on hardness. Though only a very small percentage of increase in hardness of about 7% is detected in $X_{700\text{-}5}$ when compared to $X_{700\text{-}1}$ and 5.4% increase in $X_{730\text{-}5}$ when compared to $X_{730\text{-}1}$, it can be noted that the hardness increases

to some extent due to the increase in the simulation cycles. Differences in the hardness of the samples $X_{700\text{-}1}$ and $X_{730\text{-}1}$ are also only about 8% higher in $X_{730\text{-}1}$ and only about 6% increase in $X_{730\text{-}5}$ than compared to $X_{700\text{-}5}$ which shows only a slight variation in the hardness percentage at higher temperatures. The hardness of $X_{830\text{-}1}$ is only about 955HV which is very close to the hardness of sample $X_{730\text{-}3}$.

The hardness of the untransformed pearlite in the samples simulated are shown in figure 3.15. Increase of pearlite hardness is seen in both samples X_{700} and X_{730} when compared to the base material pearlite. The pearlite hardness in $X_{700\text{-}1NS}$, $X_{700\text{-}1}$, $X_{700\text{-}5}$ and $X_{730\text{-}1}$, $X_{730\text{-}3}$, $X_{730\text{-}5}$ is about 278HV, 314HV, 331HV and 339HV, 368HV, 341HV respectively. Similar pattern seen in the hardness of martensite with temperature and cycles can be seen in pearlite. The increases in the hardness could be due to the finer interlamellar spacing of the pearlite lamellae [47,48] caused by the deformation cycles which can be seen in [49] where changes in the hardness are related to the interlamellar spacing.

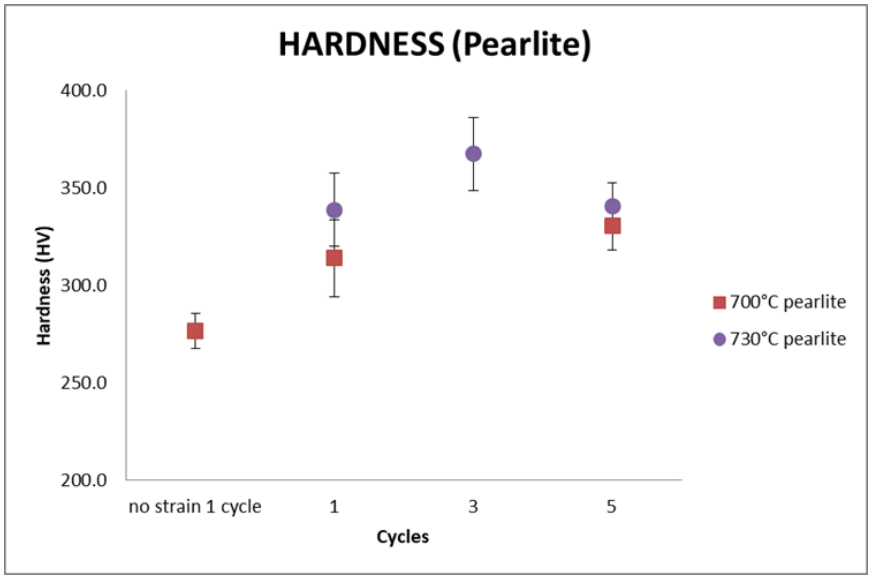

Fig: 3.15 Hardness of untransformed pearlite

3.5 Analysis of spheroidization in cementite

Spheroidization in pearlite is the change of the lamellar features of the cementite into spherical structures, though this change does not affect the consistency in the phase volume. The mechanism of spheroidization usually involves several partial processes such as fragmentation, rounding of small plate segments into spherical particles, particle coarsening and growth of ferrite grains. The main models which explain the spheroidization of cementite are (i) Rayleigh's perturbation theory, (ii) Grain boundary thermal groove theory and (iii) Fault migration theory. Though these models explain some features of the spheroidization process, there are many particulars that cannot be explained by the theories [50]. The progression of

spheroidization is non-homogenous and in samples spheroidizingly annealed it can be observed in the microstructure of these samples regions of fully spheroidized cementite areas next to very well preserved cementite lamellae regions or also whole colonies of lamellar pearlite. The reason for such behavior is unknown [51].

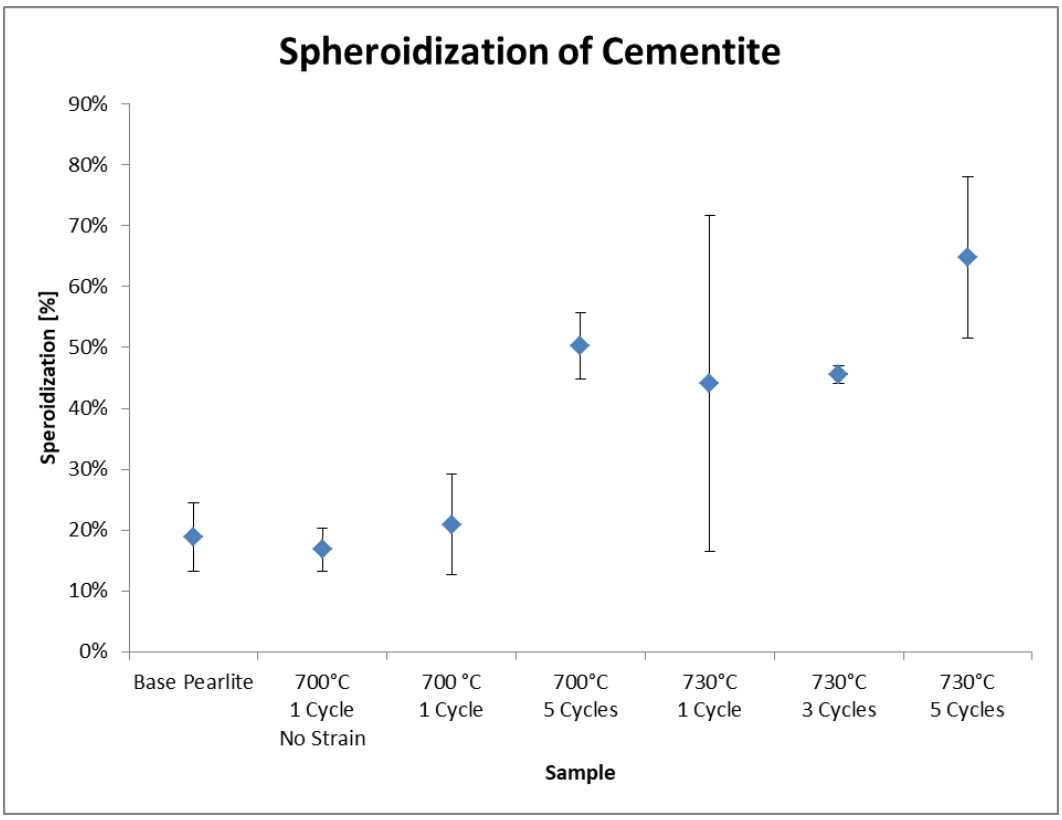

Fig: 3.16 Spheroidization of cementite in base pearlite and samples X_{700} and X_{730}

Figure 3.16 shows the spheroidization graphs estimated from the the base pearlite, X_{700} and X_{730} samples using the Imagej software which was also discussed in section 2.7. It can be seen from the figure that spheroidization is noticed also at the base pearlite microstructure (Fig. 3.1). This is an essential information that is to be noticed while analysing the spheroidization that occurs in the simulated samples. The spheroidization percentage is seen to increase with increase in temperature and cycles in the simulated samples than compared to the base pearlite. The increase is about 11% in $X_{700\text{-}1}$, 163% in $X_{700\text{-}5}$, 132% in $X_{730\text{-}1}$, 142% in $X_{730\text{-}3}$ and 242% in $X_{700\text{-}5}$ when compared to base pearlite. It is to be noted that due to the higher amount of unmeasurable areas of spheroidization sample $X_{730\text{-}1}$ has higher margin of error. The increase in the spheroidization could be due to the deformation and is same phenomenon of increase in spheroidization by deformation is noticed in [52] where high carbon rail steel specimens subjected to compressive deformation show significant increase in spheroidization.

A decrease in 10% spheroidization is seen in $X_{700\text{-}1NS}$ when compared to base pearlite due to the small sample size which fits within the to be expected margin of error.

3.6 Analysis of stress-strain curves

The stress-strain curves of the samples X_{700}, X_{730} and X_{830} are shown in Fig. 3.17. The changes in the stress-strain curves at the various stages in the cycle is indicated in the figure for the sample X_{700} as example. The "heating and deformation" limits show the stress-strain changes in the curve followed by the "end of heating and deformation" point which indicates the point where the heating is stopped and strain is withdrawn. The cooling curves are not visible but the region of cooling is indicated in the figure. From Fig. 3.17 it is observed that when temperature increases the yield limit decreases but the yielding limit of sample X_{830} is not clearly visible. The maximum stress gradually decreases with the increase of simulation temperature which could be due to the thermal softening of the material. The region between the "end of heating and deformation" and "cooling" indicates the elongation in the sample once the heating and deformation is withdrawn. As temperature increases the length of the elongation region decreases. It can be seen that the amount of plastic deformation of the samples increases with increase in temperature which is seen by the increase in strain due to the softening of the material.

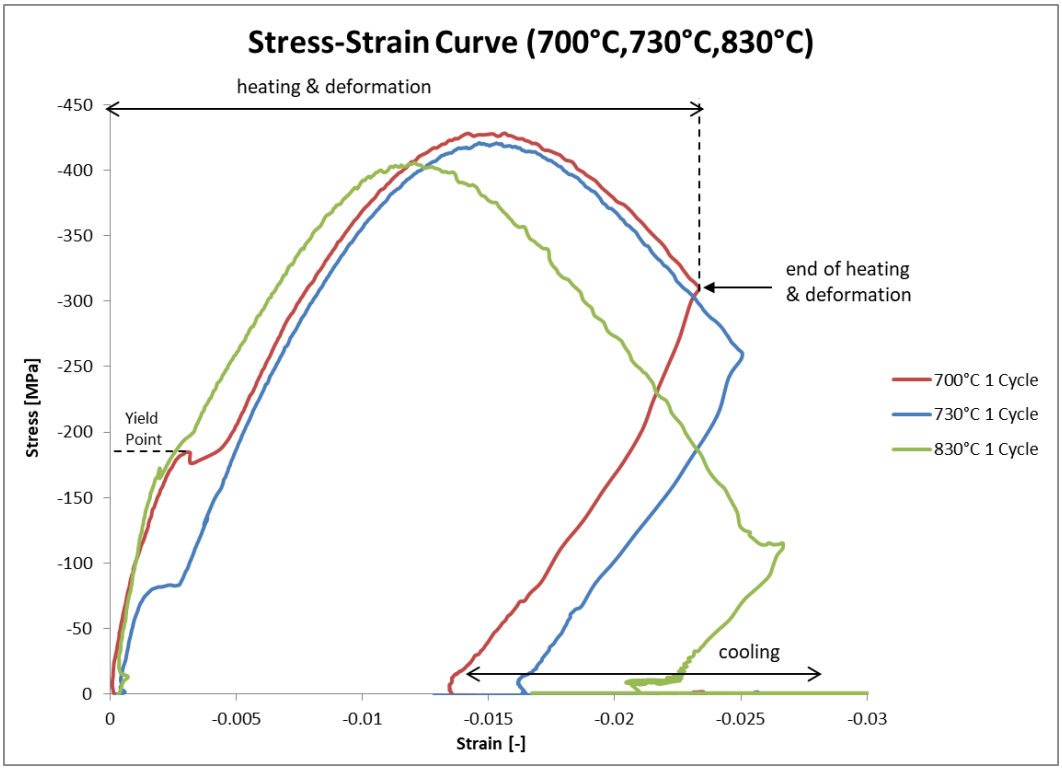

Fig:3.17 Stress-strain curves of sample X_{700}, X_{730}, X_{830}

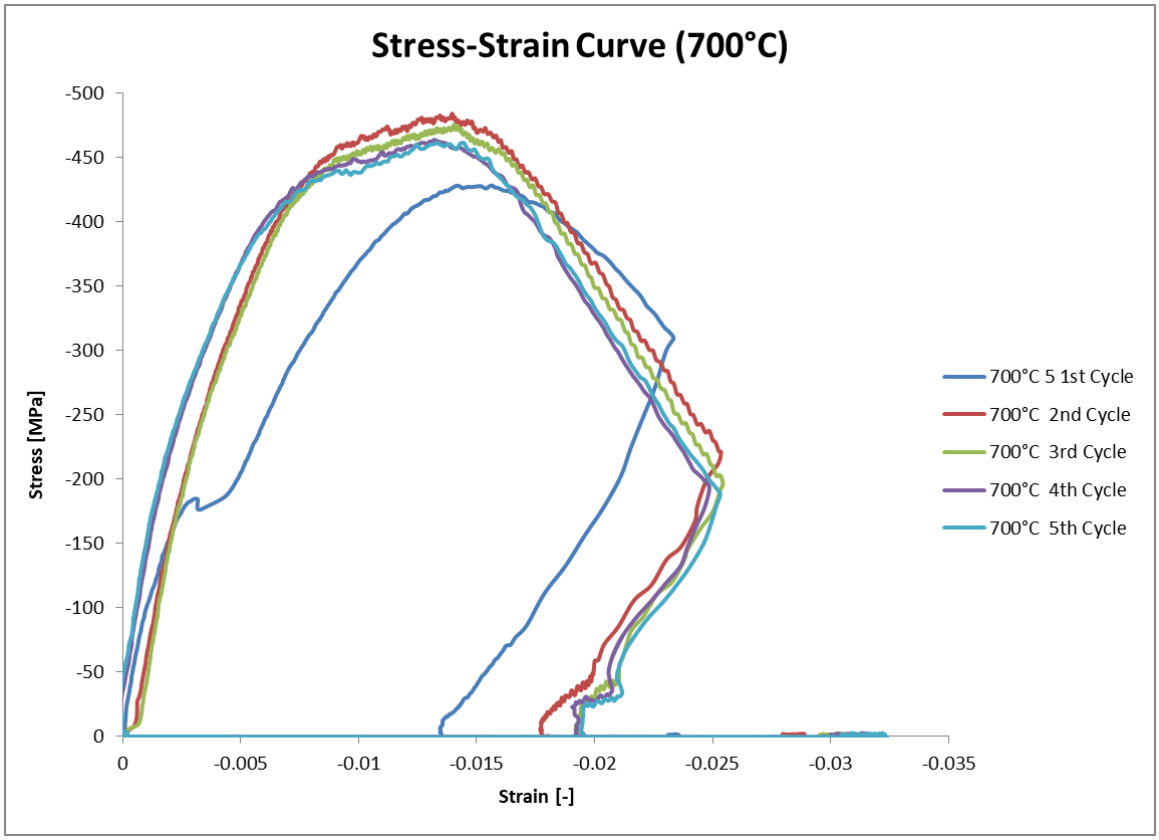

Fig: 3.18 Stress-strain curves of sample $X_{700\text{-}5}$

The stress-strain curves of sample $X_{700\text{-}5}$ is seen in figure 3.18. The stress-strain curve of the first cycle is significantly different from the rest of cycles. The maximum stress and the area under the curve representing toughness are higher in the second to fifth cycle. When the cycle increases the stress increases which could be due to the increase in strain hardening. After the second cycle the maximum stress gradually decreases which could be due to thermal softening effects overcoming the strain hardening. Similar trends regarding plastic deformation shown in Fig. 3.17 is observed here.

Most of the trends observed in the sample $X_{700\text{-}5}$ are also observed in sample $X_{730\text{-}5}$ except that maximum stress increases till the third cycle before it starts to decrease. This could be due to the increase in strain hardening .

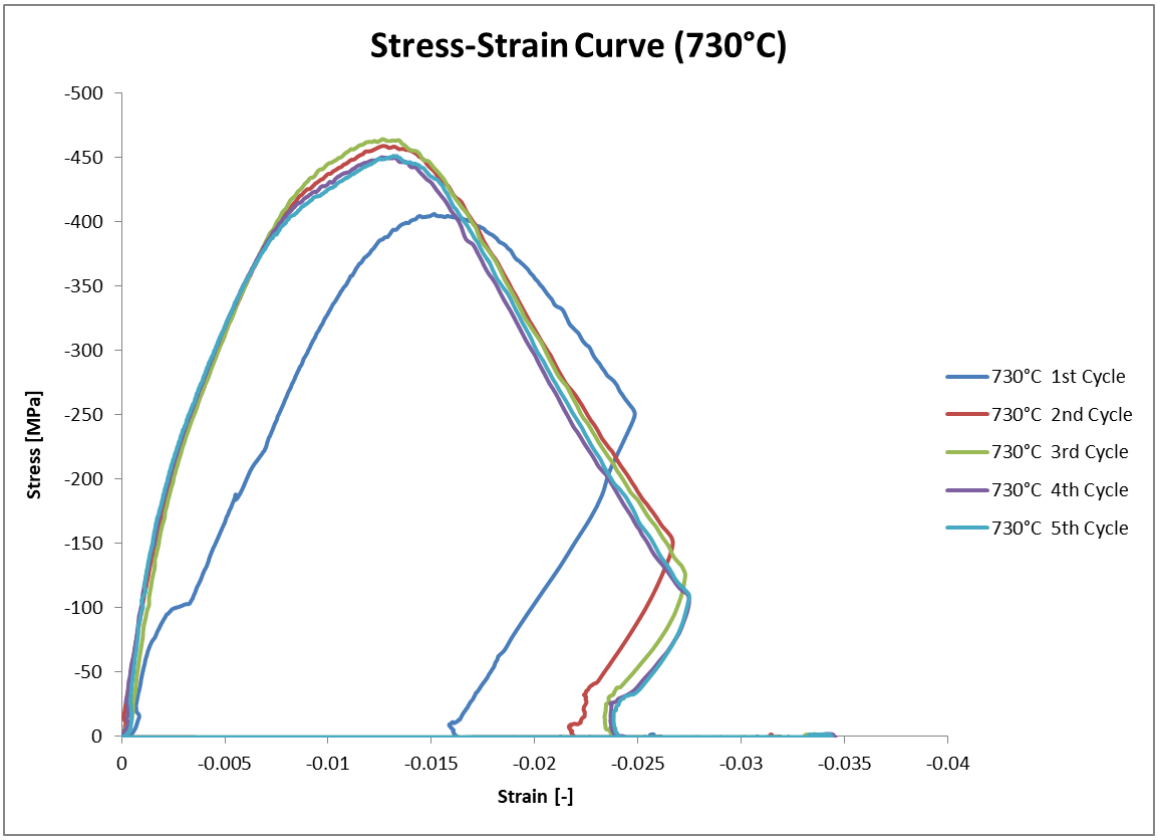

Fig: 3.19 Stress-strain curves of sample $X_{730\text{-}5}$

3.7 DISCUSSION

The friction-wear behavior between the wheel and rail systems is a very complex phenomenon which involves high mechanical loading cycling and microscopic fatigue systems [53]. During the loading cycles contact-stresses is developed between the rail-wheel system and one of the unfavorable effects from the development of contact stresses is the rolling contact fatigue defects (RCF). RCF are developed due to the plastic deformation at the rail surface due to rolling/sliding contact of one surface with the other and certain RCF defects such as squats can be frequently associated to the white etching layers (WEL) [54] .This increases the risk of crack propagation in rail surface and wheel surface [55]. These cracks are developed due to the repeated wheel loads, which suggest that the crack developed due to WEL can be called as one of RCF cracks and sometimes the squat type cracks though the crack propagation is not properly based on RCF. During the last decades efforts have been made to study the RCF defects and WEL after main derailment incidents such as the Hathfield incident in 2000. Hence the study of WEL is very necessary for the understanding of its mechanism of formation and

mechanical properties to improve the rail system and reduce the maintenance costs done on WEL.

Many studies have been done related to WEL for better understanding of the effects of heating or loading that occur during the passage of a train on the rail [17-21]. The most widespread study to mimic the contact between the wheel and rail in real life to an experiment is the twin disc experiment where a rotating disc which simulates the wheel slides over a stationary disc simulating the wheel. Though the twin disc experiment is cost effective than compared to the real time on-track investigation, most of the twin disc studies concentrate on the study of crack morphology, crack initiation and crack growth by rolling/sliding that occurs in the surfaces. Just like the twin disc experiment, most experiments focus only either on the heating aspects or deformation aspects that influence WEL formation. The thermo-mechanical simulation used in the current study discusses the thermal and mechanical effects which influence the WEL formation; the further sections discuss the effects of deformation, temperature and loading cycles that are observed in by simulation.

3.7.1 Effect of plastic deformation on pearlite to austenite formation

Generally the transformation of pearlite to austenite takes place in four steps (i) pearlite unaffected or a short incubation period (ii) nucleation and growth of austenite from pearlitic ferrite (iii) cementite transformation into austenite and (iv) diffusion of carbon from cementite-austenite interface to austenite. This transformation process starts when the temperature is increased to A_1 temperature (temperature required for austenite to pearlite eutectoid transformation). As the temperature is increased the difference between the free energy of the product phase (austenite) and parent phase (pearlite) increases and also increase the atomic mobility. Hence the increase of temperature increase the driving force for austenite formation and atomic mobility which positively affects the rate of nucleation and growth of austenite. Austenite is understood to favour the nucleation sites at the interface of the pearlite which was mentioned by many authors, austenite grains preferentially nucleate at the high angle grain boundaries between the pearlite colonies where the sureface energy is more favourable. Austenite after nucleation are noticed to grow laterally along the plates of the ferrite in a pearlite colony and expand to replace the ferrite in the colony. The cementite plates dissolve in the austenite but as the austenite growth is higher than the cementite dissolution, the cementite plate first break then completely dissolve in ausetenite. The signs of the former presence of the cementite plates are visile for a short period of time due to the in-homogenous distribution of carbon in austenite. These traces also disappear with time [51] understood from the studies of many authors to be martensite and is formed after the quenching of austenite to form the final microstructure.

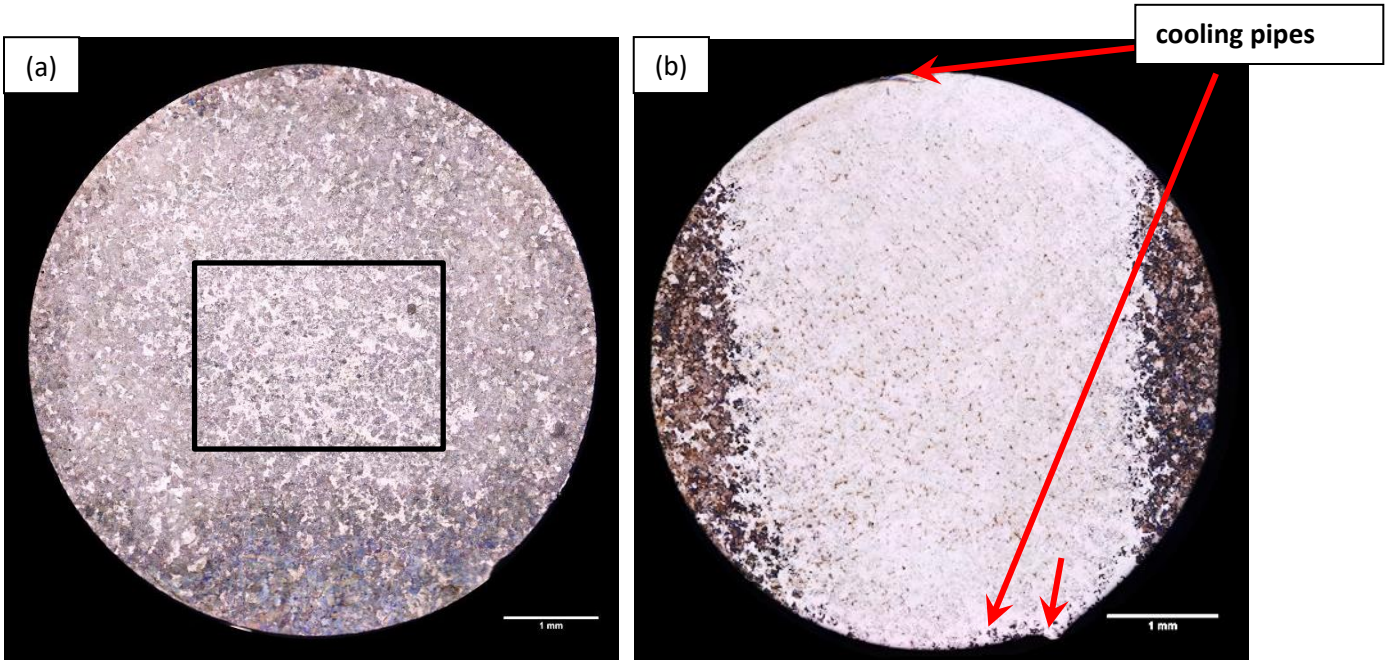

Fig.3.20 OM images of (a)$X_{700\text{-}1NS}$ and (b) $X_{700\text{-}1}$

The samples $X_{700\text{-}1NS}$ and $X_{700\text{-}1}$ simulated can be used to analyse the effects of deformation on WEL formation. The samples were simulated with the same parameters such as heating rate, cooling rate and maximum temperature of the heating cycle but without compressive strain in $X_{700\text{-}1NS}$ and with compressive strain $X_{700\text{-}1}$.The overview of the samples seen in Fig. 3.20(a and b) shows the pearlite and martensite phases present in the sample. In sample $X_{700\text{-}1NS}$ (Fig. 3.20a) the martensite formed is about 9% which is predominantly at the middle region of the sample indicated by the rectangle area. The amount of martensite formed is visibly higher of about 63%, it can be also noted that the untransformed pearlite is situated on both ends of the position where the thermocouple was placed previously placed indicated by the arrow (Fig. 3.20b). This position also corresponds to the position of the cooling pipes both sides of the sample indicated by the arrows, which could possibly indicate that presence of untransformed pearlite on either side of the cooling pipe location due to incomplete transformation of pearlite to austenite seen as dark regions.

The increase in the WEL percentage by deformation could indicate that temperature increase is due to plastic deformation, to understand the heat increase while simulating the $X_{700\text{-}1NS}$ with strain,simulation was done by fixing two thermocouples to measure temperature at the surface and at the core of the sample and the a single cycle with simultneous heating and straining was done. The results from the experiment is shown in Fig. 3.21. It can be seen that the temperature increase at the middle region (core) is about 23°C. From the equilibrium quasi-binary iron-carbon phase diagram calculated in the study conducted by Jun Wu et.al [20] on the same rail material it can be seen that the minimum temperature for austenite to form (Ac_1) is

about 700°C and the full austenization temperature (Ac_3) is about 722°C. This explains the minimum and maximum amount of WEL formation in $X_{700\text{-}1NS}$ and $X_{700\text{-}1}$ (9% and 63%) respectively. From Fig. 3.21 it can also be observed that the core heats up quicker which in sample X700-1NS would assist in the higher austenite nucleation in the base pearlite and subsequently martensite while cooling.

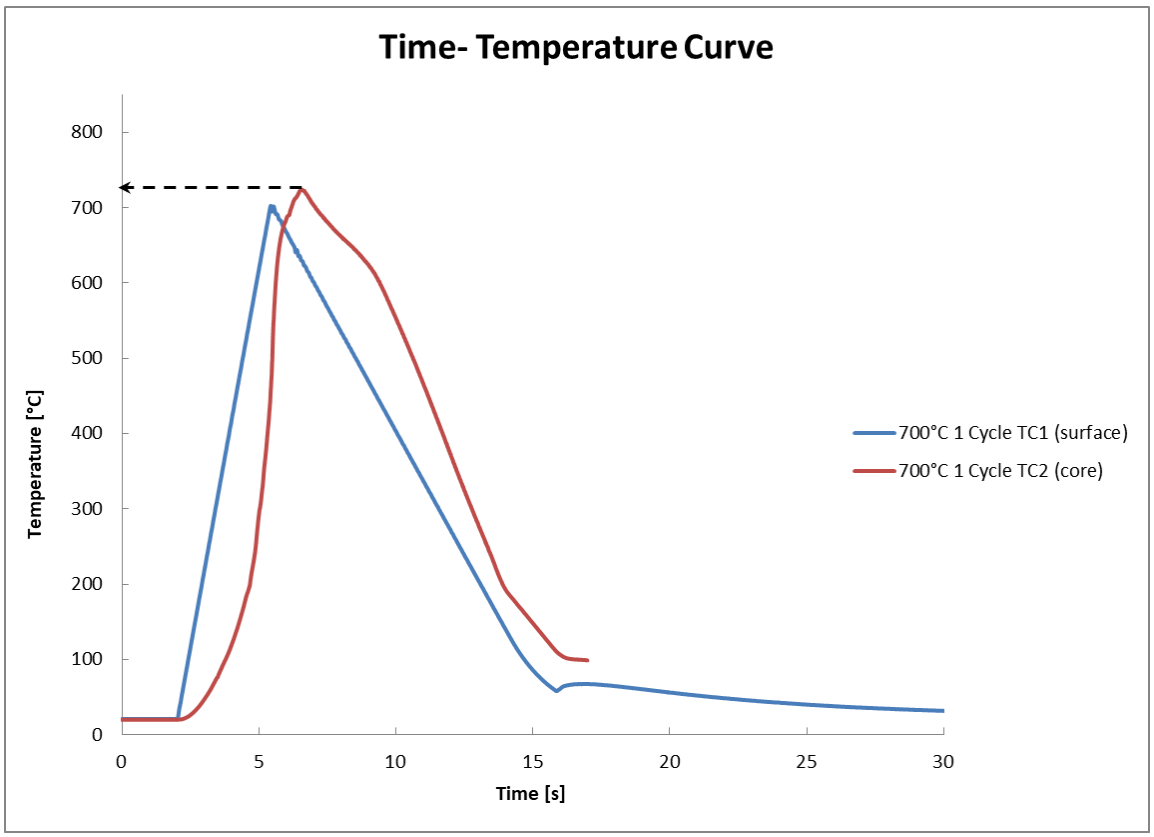

Fig: 3.21 Time-Temperature curves of $X_{700\text{-}1}$

3.7.2 Effects of temperature and cycles on WEL formation

The transformation of austenite increases as the temperature increases, in sample X_{700} this pattern is evident from the optical microscopy images of the sample and the quantification of the phases in all the cycles showed an increase in martensite with respect to the previous cycle. In samples X_{730} the results do not display the ascending pattern seen in X_{700} due to the excessive banding structure that covers the samples which becomes severe as the cycles increase. The banding checked with EPMA does not show isolation of alloying elements such as Mn which causes banding structure as studied in literature [46]. The exact causes for the bands formed are unknown and results from another set of the same experiments performed initially also display bands in the microstruture as seen in Fig. 3.8d. The repetition of the bands on both

sets of experiments show that errors probably occurred during the simulation process due to in-homogenous heating or error in the deformation cycles. More studies have to be done on the formation of martensite at 730°C to conclude on the causes of the bands. Although the amount of martensite formed is lower in X_{730} than compared to X_{700}, it can be noticed that hardness of the samples X_{730} increases with each cycle. The hardness increase could be due to the increase of carbon content in the austenite, and the subsequently formed martensite, from the dissolved cementite [50]. From the hardness results in Fig. 3.14a, it is observed that the hardness of martensite formed increases as the simulation cycles increase. The hardness of the samples X_{700} and X_{730} is in the same range as the hardness examined from the WEL formed in a removed section of rail mentioned in [20].

Also to be spotted is the increase in the spheroidization of cementite in the samples when compared to the base material. The spheroidization occurs due to the reduction in the surface energy of the system but the process can be sped up due to deformation as mentioned in[56]. The spheroidization of cementite in samples X_{730} is seen to be higher than compared to X_{700} samples. From the SEM images in Fig. 3.7d the numerous spheroids can be observed unlike in x_{700} samples. Hence higher heating temperature combined with deformation speeds up the spheroidization of the cementite. In samples processed at temperatures higher than Ac_3 it can be noticed that SEM images of the WEL formed at 830°C (Fig. 3.11d) have less negligible traces of the cementite lamellae position in the WEL which is seen in samples processed at lower temperatures. This suggests that almost complete dissolution of cementite happens when simulated at 830°C and the WEL formed is very similar to the WEL studied directly from the removed section of rail discussed in [20].

The effect of the simulation cycles can be seen in stress-strain curves (Fig. 3.18, 3.19), The yield point of the cycle is seen to increase from the second cycle which could be related to the decrease in grain size. The stress also increases in the first few cycles due to the work hardening in the sample by the compressive strain provided. Gradual reduction in the stresses indicate softening of the material which show the possibility of recrystallization of the material.The stress-strain curves The results from the current study when compared to the thermo-mechanical simulation done on the same material in [20] shows that WEL can be sucessfully simulated at higher heating rates with three percent of effective plastic strain even with a single simulation cycle.

CONCLUSION

A study on the formation of white etching layer in rail steel R260Mn by thermo-mechanical simulation was performed by varying the maximum heating temperature from 650°C to 830°C and also varying the no. of cycles of thermo-mechanical simulation with maximum plastic strain of 3%. Metallurgical characrterization was performed to analyze the effect of temperature and deformation on the simulated WEL. The following conclusions are derived from the experimental investigatons.

- The amount of martensite formed in sample ($X_{700\text{-}1NS}$) simulated without strain increases from 9% to 63% in sample ($X_{700\text{-}1}$) simulated with strain.
- Increase in the number of simulation cycles results in increased amount of WEL formed except in sample $X_{730\text{-}5}$.
- Permanent deformation increases when maximum simulation temperature increases.
- The highest amount of martensite (95%) is formed in the thermo-mechanically simulated sample at 830°C. The corresponding microstructure is similar to the microstructure of the rail WEL reported by Jun Wu et.al [20].
- The hardness measured in the thermo-mechanically simulated samples is well within the range of micro-hardness of the rail WEL reported in [20].
- Analysis on the band like features observed in samples $X_{730\text{-}1}$, $X_{730\text{-}3}$ and $X_{730\text{-}5}$ shows no precise Mn segregation.

RECOMMENDATIONS FOR FUTURE WORK

Based on the results of the present research, the formation of WEL by thermo-mechanical simulation looks promising and future research is worth pursuing. Some recommendations for future research and experiments are given below.

- Prediction of amount of WEL formed due to the thermo-mechanical cycles and FEM analysis for temperature rise in the material due to plastic deformation can be performed.
- Detailed EBSD studies can be carried out to analyze the effect of thermo-mechanical simulation on grain size of WEL and its orientation.
- Effect of deformation on the dislocation density due to the variation of simulation cycles can be studied further using transmission electron microscopy (TEM).
- The causes for the formation of banding like structure present in samples X_{730} can be analyzed.
- Future studies on the simulation of WEL by increasing the no. of cycles and decreasing the temperature can be attempted to identify the possibility of formation of WEL.
- Studies on the amount of carbon dissolution with the increase in cycles can be attempted to analyze the trend of carbon dissolution.

REFERENCES

1) Nkundineza, Celestin, "*Influence of spatial variations of railroad track stiffness and material inclusions on fatigue life*" (2015)
2) Uwe Zerbst, Katrin Mädler, Hartmut Hintze,"*Fracture mechanics in railway applications—an overview",*Engineering Fracture Mechanics,Volume 72, Issue 2,2005,Pages 163-194.
3) European Union for Railways "*Railway Safety Performance in the European Union*"(2016) Pg22
4) Prof. Mark Robinson, Pat Scott, Bernard Lafaix, Grigory Kozyr, Allan Zarembsk, Gordana Vasic, Francis Franklin, Ben Gilmartin, Andreas Schoebel and Burchard Ripke "*Summary report and database of derailments incidents*", (October2011) ,Pg9-10
5) Zoeteman, A., Dollevoet, R., Fischer, R., & Lammers, J.-W. (2009). 28 – Managing the wheel–rail interface: the Dutch experience. *Wheel–Rail Interface Handbook*, 792–818.
6) Stuart L. Grassie, "*Rolling contact fatigue on the British railway system: treatment*", Wear, Volume 258, Issues78, 2005, Pages 1310-1318. https://doi.org/10.1016/j.wear.2004.03.065.
7) Magel, E., Mutton, P., Ekberg, A., & Kapoor, A. (2016). NRC Publications Archive Archives des publications du CNRC Rolling contact fatigue , wear and broken rail derailments.
8) NSW. (2012). *Rail Defects Handbook: TMC 226*, 1–83. https://doi.org/http://extranet.artc.com.au/docs/eng/track-civil/guidelines/rail/RC2400.pdf
9) Cannon, D. F., Edel, K. O., Grassie, S. L., & Sawley, K. (2003). *Rail defects: An overview. Fatigue and Fracture of Engineering Materials and Structures*, 26(10), 865–886.
10) U.S. Department of Transportation, F. R. A. (2011). Rolling Contact Fatigue: A Comprehensive Review, (November). Retrieved from https://ntl.bts.gov/lib/43000/43400/43400/TR_Rolling_Contact_Fatigue_Comprehensive_Review_final.pdf
11) Dollevoet, R. P. B. J. "*Design of an Anti Head Check profile based on stress relief"*. 2010, https://doi.org/10.3990/1.9789036530736.
12) Dirks, B., Transportation, B., Deterioration, R., View, P., & Dirks, B.. "*Simulation and measurement of wheel on rail fatigue and wear Simulation and measurement of wheel on rail fatigue and wear",* (2016).
13) Meysam Naeimi , Zili Li and Rolf Dollevoet, "*Nucleation of squat cracks in rail, calculation of crack initiation angles in three dimensions*", Journal of Physics: Conference Series 628 (2015)
14) Robin Andersson, "*Surface defects in rails*",2015
15) Dr W. Daniel, *"Final Report on the Rail Squat Project R3-105"*, (2013)
16) Grégory Antoni *"A phenomenological modeling with thermo-mechanical coupling for Tribological Surface Transformations (TSTs)"*, International Journal of Engineering Science Volume 78, May2014, Pages218-232.
17) Carroll, R. I., & Eng, M. (2005)." *Surface Metallurgy and Rolling Contact Fatigue of Rail"*, (December).
18) Minoru Umemoto, Yoshikazu Todaka, Akifumi Akifumi Ohno , Mayumi Suzuki and Koichi Tsuchiya ,"*Dissolution of Cementite in Carbon Steels by Heavy Deformation and Laser Heat Treatment"*, Materials Science Forum, Vols. 503-504, pp. 461-468, 2006 https://doi.org/10.4028/www.scientific.net/MSF.503-504.461

19) Carroll, R. I., & Beynon, J. H. (2007). Rolling contact fatigue of white etching layer: Part 1. Crack morphology. *Wear*, *262*(9–10), 1253–1266. https://doi.org/10.1016/j.wear.2007.01.003\
20) J. Wu, R.H. Petrov, M. Naeimi, Z. Li and J. Sietsma*," A Microstructural Study of Rolling Contact Fatigue in Rails"* The Second International Conference on Railway Technology: Research, Development and Maintenance, Paper118 (2014)
21) Takahashi, J., Kawakami, K., & Ueda, M. (2010). Atom probe tomography analysis of the white etching layer in a rail track surface. *Acta Materialia*, *58*(10), 3602–3612. https://doi.org/10.1016/j.actamat.2010.02.030
22) Vivek M. Rosario, *"Production of a thermal barrier material by combustion synthesis"* , 1998, 34-35.
23) https://www.gleeble.com/about-us1/company-history.html
24) https://camm.osu.edu/facilities/processing/gleeble%E2%84%A2
25) Douglas B. Murphy, "Fundamentals of Light Microscopy and Electronic Imaging", Pg1-3
26) Eliva L. Levi "Practical Hardness testing made simple", 14-16. https://app.aws.org/educators/Library/0000/000587.pdf
27) http://www.csun.edu/~bavarian/Courses/MSE%20528/microindentation_hardness_testing.pdf
28) https://www.twi-global.com/technical-knowledge/job-knowledge/hardness-testing-part-1-074/
29) https://www.nanoscience.com/technology/sem-technology/sem-components/
30) Joseph Goldstein, Dale E. Newbury, David C. Joy, Charles E. Lyman, Patrick Echlin, Eric Lifshin, Linda Sawyer, J.R. Michael "Scanning Electron Microscopy and X-ray Microanalysis" Third Edition, Pg1-5.
31) Fu-Yun Zhu, Qi-Qi Wang, Xiao-Sheng Zhang, Wei Hu, Xin Zhao and Hai-Xia Zhang "*3D nanostructure reconstruction based on the SEM imaging principle, and applications*" Nanotechnology Volume25,
32) http://iopscience.iop.org/article/10.1088/0957-4484/25/18/185705/meta
33) https://serc.carleton.edu/research_education/geochemsheets/techniques/SEM.html
34) http://blog.phenom-world.com/sem-electrons-detection-provide-information
35) https://www.quora.com/What-is-electron-microscopy
36) https://serc.carleton.edu/research_education/geochemsheets/techniques/EPMA.html
37) https://www.cameca.com/products/epma/technique
38) Xavier Llovet "*Electron probe microanalysis: principles and application*" http://diposit.ub.edu/dspace/bitstream/2445/32146/1/MT04%20-%20Electron%20Probe%20Microanalysis%20_ed2.pdf
39) *"Electron probe microanalysis"* Cameca, Ametek https://rsc.aux.eng.ufl.edu/_files/documents/1.pdf
40) Nilanjan Chatterjee "*Electron Microprobe Analysis*", MIT, January 2012, Pg. 4 https://ocw.mit.edu/courses/earth-atmospheric-and-planetary-sciences/12-141-electron-microprobe-analysis-january-iap-2012/lecture-notes/MIT12_141IAP12_coursenotes.pdf
41) https://imagej.nih.gov/ij/docs/intro.html
42) Arruabarrena, J. (2011). "*Carbide spheroidization kinetics in a low alloy medium carbon steel : Relevance of deformation after transformation"*, (January 2014), Pg. 699

43) Chattopadhyay, S., & Sellars, C. M. (1977). *Quantitative measurements of pearlite spheroidization.* Metallography, *10*(1), 89–105. https://doi.org/10.1016/0026-0800(77)90044-1
44) M. Naeimi, Z. Li, R. Dollevoet, J. Wu, R.H. Petrov and J. Sietsma, "*thermo-mechanical effects in the formation mechanism of rail squats*" The third International Conference on Railway Technology: Research, Development and Maintenance, Paper252.
45) http://www.railwayrail.com/products/54e1-uic860-standard-steel-railuic-54-steel-rail/
46) Ted F. Majka, David K. Matlock, George Krauss *"Development of Microstructural Banding in Low-Alloy Steel with Simulated Mn Segregation"*, METALLURGICAL AND MATERIALS TRANSACTIONS A, Volume 33A, June 2002
47) Atom probe study on microstructure change in severely deformed pearlitic steels: application to rail surfaces and drawn wires Jun Takahashi
48) https://vacaero.com/information-resources/metallography-with-george-vander-voort/1437-the-interlamellar-spacing-of-pearlite.html
49) Extremely Fine Pearlite by Continuous Cooling Transformation K. M. Wu a,b H. K. D. H. Bhadeshia
50) Stability of a lamellar structure – effect of the true interlamellar spacing on the durability of a pearlite colony (http://www.imim.pl/files/archiwum/Vol4_2015/06.pdf)
51) Tian, Y. L., & Kraft, R. W. (1987). Mechanisms of Pearlite Spheroidization. *Metallurgical Transactions A*, *18*(8), 1403–1414. https://doi.org/10.1007/BF02646654
52) Handa, K., Kimura, Y., Yasumoto, Y., Kamioka, T., & Mishima, Y. (2010). Effect of deformation and annealing temperatures on ultrafine microstructure development and yield strength of pearlitic steel through continuous recrystallization. *Materials Science and Engineering A*, *527*(7–8), 1926–1932. https://doi.org/10.1016/j.msea.2009.11.036
53) Baumann, G., Fecht, H. J., & Liebelt, S. (1996). Formation of white-etching layers on rail treads. *Wear*, *191*(1–2), 133–140. https://doi.org/10.1016/0043-1648(95)06733-7
54) Andersson, R. (2015). Surface defects in rails, 30.
55) Ishida, M., & Maruyama, Y. (2015). Detection of White Etching Layer Causing Rail Defects. *10th International Conference on Contact Mechanics CM2015, Colorado Springs, Colorado, USA*.
56) Takahashi, J. (2017). Atom probe study on microstructure change in severely deformed pearlitic steels: Application to rail surfaces and drawn wires. IOP Conference Series: Materials Science and Engineering, 219(1). https://doi.org/10.1088/1757-899X/219/1/012007